OTR based measurements for ELI-NP Gamma Beam Source

Facoltà di Scienze Matematiche Fisiche e Naturali

Dottorato di Ricerca in Fisica degli Accelleratori – XXXI Ciclo

Candidate
Maco Marongiu
ID number 1689676

Thesis Advisor
Prof. L. Palumbo

Co-Advisor
Prof. A. Mostacci

June 2019

Thesis defended on 13 September 2019
in front of a Board of Examiners composed by:

Prof. D' Angelo Annalisa (chairman)
Prof. Senesi Roberto
Prof. Antici Patrizio

OTR based measurements for ELI-NP Gamma Beam Source
Ph.D. thesis. Sapienza – University of Rome

Author's email: marco.marongiu@uniroma1.it

Contents

List of Symbols

Chapter 1

Introduction

Optical Transition Radiation (OTR) monitors are widely used for profile measurements at Linacs. The radiation is emitted when a charged particle beam crosses the boundary between two media with different optical properties, here a thin reflecting screen and vacuum. For beam diagnostic purposes the visible part of the radiation is used and an observation geometry in backward direction is mainly chosen which corresponds to the reflection of virtual photons at the screen which acts as mirror.

Advantages of OTR are the instantaneous emission process enabling fast single shot measurements, and the good linearity (when the coherent component is negligible); disadvantages are that the process of radiation generation is invasive (i.e. a screen has to be inserted in the beam path) and that the radiation intensity is much lower in comparison to scintillation screens. For high intensity electron beams the interaction of the beam with the screen material may lead to a screen degradation or even a damage (see section 1.1.1).

The angular distribution of OTR can also be exploited due to the fact that the angular distribution possesses characteristic maxima at angles $1/\gamma$ with γ the Lorentz factor: from such a measurement the beam energy can be therefore derived (see section 1.1.3).

The Gamma Beam Source (ELI-NP-GBS) machine is an advanced source of up to ≈ 20 MeV Gamma Rays based on Compton back-scattering, i.e. collision of an intense high power laser beam and a high brightness electron beam with maximum kinetic energy of about 720 MeV. The Linac will provide trains of 32 electron bunches in each RF pulse, separated by 16.1 ns; each bunch has a charge of 250 pC .

The goal of my work is to propose a layout for a distributed energy measurement along the ELI-NP-GBS machine: this will be useful during the commissioning stage of the machine in order to verify the correct functionality of the newly design C-Band accelerating structures, due to the fact that there are OTR screens after each accelerating module. Furthermore, I have studied the feasibility of bunch by bunch energy measurement using a gated camera system.

Moreover, the possibility to perform fast single shot measurements could be very useful in plasma based accelerators (i.e. EuPRAXIA@SPARC_LAB), where the compactness requirement and especially a large shot to shot energy jitter may lead to issues in the use of a conventional spectrometer.

1.1 Layout Characterization

The first part of my work has consisted in a series of studies aimed to characterize the whole measurement layout; therefore, I performed a thermal study on the two mainly used materials for the OTR screen (silicon and aluminum) to find out what material best fit the ELI-NP-GBS requirements both in terms of thermal resistance and in terms of quality of the imaging.

Then, I studied the optical system in terms of intensity radiation (how many photons are emitted by the screen and how many are collected by the optical system) and in terms of resolution and magnification (and how this parameters affect the accuracy).

Finally, I performed an analysis of data taken from SPARC_LAB in order to study how the fitting routines behave with experimental data which are close to the ones of some diagnostic stations in the ELI-NP-GBS; this study allows to find some critical issues (i.e. the effect of the Signal to Noise Ratio (SNR) to the accuracy of the fit).

1.1.1 Thermal Analysis

When a beam hits a surface, it deposits an amount of energy ΔE which causes an instantaneous temperature increase: such increase depends linearly on the bunch charge and inversely on the specific heat and the size of the beam. Therefore, a more dense beam causes more heating. The study I performed

on aluminum and silicon screens (400 μm thick) shows both analytically and numerically (ANSYS) a high temperature increase [1]: this is not critical from the thermal point of view since the screen temperature stays well below the melting point of the material, but it could be critical from the mechanical point of view (i.e. alternate stress due the the cyclic thermal loads).

Further fatigue analysis based on the Equivalent Von Mises Stress [2] showed that the aluminum screens last less than 2 h of operation in the case of the more dense beam of the ELI-NP-GBS, while the silicon screen showed no issue; furthermore, this drawback is strictly related to the full 32 bunches. Indeed, with a train of 16 bunches also the aluminum screens showed no time limitation.

The resolution requirements limits the choice of suitable screens materials due to the necessary good planarity and low roughness; indeed, other facilities deal with this kind of thermal issue, but the solution adopted by them (i.e. at CLIC tungsten screens are used) does not give the necessary resolution.

For this reason, the silicon has been proposed as the OTR screen material: this cause further considerations in terms of radiation intensity that are analyzed in 1.1.2.

1.1.2 Imaging System

Other aspects to take into consideration for an accurate measurement are related to the optical system: so, taking into account the geometry constraints of the machine, a study of possible optical layout and the achievable magnification and resolution has been performed [3]. This study is important due to the fact that the beam envelope in the ELI-NP-GBS Linac is expected to vary from about 1 mm at the gun injection to 10 μm at the interaction point; so, each diagnostic station may require different field of view and resolution. Therefore, I have evaluated the resolution and the magnification achievable and the effect of the finite resolution on the accuracy of the measurements. Another study, presented at the IBIC 2017 Workshop, aims to evaluate the collecting efficiency of the optical system; both studies refers to the case of OTR far field regime.

1.1.3 Energy Measurements

The OTR angular distribution of a single particle, also called Single Particle Function (SPF), has a center minimum equal to zero, and two maxima; the distance of these two maxima is inversely proportional to the particle energy. However, when the beam angular distribution is observed, also the beam divergence need to be taken into account: the main effect is to shift up the minimum from zero to a value which could be close to the maximum.

Assuming a gaussian distribution of the beam divergence, one can convolute this distribution with the SPF and retrieve a fitting equation that can allow to measure beam energy and beam divergence. I have performed this analysis using data taken from the SPARC_LAB facility in order to evaluate the accuracy of the measurement in different working conditions (i.e. single shot measurement, different values of energy, charge and divergence). The results have been presented at the EAAC Workshop.

Another possible measurement could be the energy measurement of a plasma accelerated beam (i.e. EuSPARC@SPARC_LAB) thanks to the single shot possibility of this measurement technique: the large energy jitter, indeed, could lead to inaccurate measurement with conventional techniques. In this case, however, one must take into account the contribution given by the energy spread.

1.2 Goal of the Thesis

The main goal of the thesis is to propose a layout for a distributed energy measurement along the ELI-NP-GBS machine. In order to correctly perform the measurements, few improvements need to be done to the optical layout: for instance, by adopting a specific optical layout one could increase the resolution or the magnification or the depth of field or, more in general, the overall performance of the diagnostic system.I performed these studies also with simulation software like Zemax.

Furthermore, in order to perform the measurement of a single bunch of the train using a gating camera and an intensifier (i.e. "Hamamatsu Orca-Flash4"), I have characterized the camera in order to find the optimum gain value for each working point to avoid a bad SNR or saturation. Both the situations could compromise the measurement accuracy.

Chapter 2

ELI-NP

Recent developments in particle accelerators and lasers technology opened new perspectives for the realization of new X and γ ray sources through electron-photon collision. These sources are based on the inverse Compton scattering effect, in which a high brightness electron beam scatters an intense high power laser beam, converting optical photons ($E_{ph} \approx$ eV) into energetic photons ranging from KeV to MeV.

The idea of using Compton scattering to generate a high energy X-Ray or γ-Ray beam was first proposed in 1963 by Milburn [4] and Arutyunian [5]. The LADON project [6] has been the first facility to produce a monochromatic polarized gamma beam exploiting the collision of a laser with the electrons from the ADONE storage ring [7] in Frascati. Nowadays several test facilities, that generate γ-Ray beams by means of Compton scattering are present in different laboratories worldwide [8, 9, 10, 11, 12, 13], together with newly conceived user facilities [14, 15, 16, 17]. This is true both for X-Ray sources, which are primarily used for advanced imaging techniques, and for the γ-Ray sources used for research in nuclear physics and industrial purposes. They found their natural interest in imaging and nuclear fundamental physics, but their potential application range extends to a large number of fields: medicine, biology, material science, cultural heritage, national security and high energy physics.

Photon beams generated by Compton scattering have been successfully used for the implementation of biological computer aided imaging techniques, like for instance phase-contrast tomography at the Munich Compact Light Source [15, 18]. This has been possible thanks to small round source spot size,

high spatialand temporal resolution, and the quasi-monochromaticity typical of these sources. Moreover, with respect to the conventional X-Ray tubes, the absence of low energy tails in the photon spectrum, allows edge enhancement with an overall improvement in the image contour visibility. In particular in the medical field, mammography with mono-chromatic X-Rays at 20 KeV has been proven far superior in signal to noise ratio with respect to conventional mammographic tubes, with a considerably lower radiation dose to the tissue.

The generation of photons in the gamma range ($E_{ph} > 1\,\text{MeV}$) is particularly interesting for nuclear physics applications, e.g. the Nuclear Resonance Fluorescence technique [19, 20] based on the nuclear absorption and subsequent emission of high energy photons. This technique provides a versatile method of non-destructive analysis of both radioactive and stable nuclides. Therefore, it finds application for nuclear waste remote sensing and diagnostics, special nuclear material recognition for national security but also in isotope sensitive imaging for medical and cultural heritage purposes. Moreover, several research fields in nuclear physics and astrophysics dealing with fundamental nuclear structure studies such as nucleo-synthesis, clustering phenomena in light nuclei, photo-disintegration cross-sections measurements and photo-fission phenomena will be possible with such advanced gamma sources.

2.1 Inverse Compton Scattering

The physics of the inverse Compton scattering effect has been studied extensively and can be described through two different models [21]: classical model and a linear quantum model. In the former the laser pulse field acts as an electromagnetic undulator: like in a Free Electron Laser (FEL), the electrons oscillating in this field produce spontaneous emission radiation. This model considers all the collective effects (multi-photon absorption/emission) explaining the beam-laser pulse interaction, but it does not conserve energy and momentum. In order to take into account the quantum effects and how they impact on the quality of the produced secondary beam, the linear quantum approach is used. It is based on the relativistic kinematics and allows to predict the final characteristics and performances for a high energy Compton source.

As reported in [14], in the laboratory frame shown in Figure 2.1 the energy E_γ of the scattered γ-Ray, propagating in the direction given by the polar
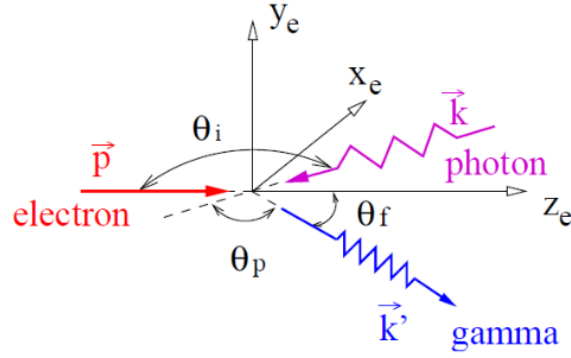
Figure 2.1. Sketch of Compton scattering of an electron and a photon in the laboratory frame: the electron is moving along the z_e direction while the incident photon is propagating along the direction given by the polar angle θ_i and the azimuthal angle ϕ_i. The collision happens at the origin of the coordinate system, and the scattered γ ray propagates in the direction given by the polar angle θ_f and the azimuthal angle ϕ_f. θ_p is the angle between the momenta of incident and scattered photons, while the electron after the collision is not shown in the figure.

angle θ_f, can be expressed by:

$$E_\gamma = \frac{(1 - \beta \cos \theta_i) E_p}{1 - \beta \cos \theta_f + (1 - \cos \theta_p) E_p / E_e}, \tag{2.1}$$

where $\beta = v/c$ is the ratio of the incident electron velocity relative to the speed of light, E_e and E_p are the energy of the electron and optical photon before scattering, θ_i is the angle between the momenta of the incident photon and the electron and θ_p is the angle between the momenta of the incident and scattered photons.

In case of head-on collision ($\theta_i = \pi$ and $\theta_p = \pi - \theta_f$) and ultra-relativistic electron, the photon is scattered into a cone with a half-opening angle equal to the inverse of the Lorentz factor γ along the direction of the incident electron. For a small scattering angle, the Equation 2.1 can be simplified to:

$$E_\gamma \approx \frac{4\gamma^2 E_p}{1 + \gamma^2 \theta_f^2 + 4\gamma^2 E_p / E_e}, \tag{2.2}$$

in which the last term in the denominator accounts for the so called electron recoil effect and it is responsible for the correct energy and momentum conservation in the scattering reaction. This term, that affects the performances of

the emitted photon beam, is negligible for X-Ray Thomson Sources, while it is small but not negligible for higher energy Compton Sources, and becomes the dominant term for deep Compton Sources. In general, it is possible to identify three different regimes:

- **Thomson elastic regime**: negligible electron recoil;

- **Quasi-elastic Compton regime**: small but not negligible recoil;

- **Quantum Compton regime**: dominant electron recoil.

As shown by Equation 2.2, the photon energy gain factor in the inverse Compton scattering mainly depends on the energy of the colliding electron beam. This beam can be generated by a normal conducting linear accelerator (Linac), a storage ring or a superconducting Linac. Compton sources are easily tunable and their photon beam energies can be extended to cover a wide range from soft X-Ray to very high energy γ-Ray. Due to a high energy gain factor, the Compton sources are considered the most effective "photon accelerators", able to produce high power radiation with a required electron beam energy, dimensions and costs significantly lower than those of a synchrotron light source. Furthermore, secondary photons emitted by inverse Compton scattering present an energy-angle correlation. Hence, by using a collimation system, it is possible to obtain a quasi-monochromatic photon beam, while the forward focusing ensures high spectral densities in small bandwidths. Compared with a Bremsstrahlung beam which is characterized by a broadband spectrum, a Compton beam is narrowly peaked around the desired energy. Another important feature is the preservation of the laser polarization in the scattered photons. Hence, the photon beams produced with this scheme can be highly polarized, and their polarization is controlled by the one of the incident photon beam.

2.2 ELI-GBS Project

A new Compton source operating in the gamma energy range (0.2-19.5 MeV) is presently under construction in the framework of the Extreme Light Infrastructure Nuclear Physics Gamma Beam System (ELI-NP-GBS) project. The ELI-NP-GBS project [22, 23, 24] consists in the realization and commissioning

of a γ-Ray source that will be hosted in Magurele, near Bucharest (Romania). The design of this machine has been performed by the EuroGammaS association [25] which gathers academic and research institutions together with commercial companies: Istituto Nazionale di Fisica Nucleare, Università di Roma "La Sapienza", the Centre National de la Recherche Scientifique, ACP S.A.S., Alsyom S.A.S., Comeb Srl and ScandiNova Systems AB. This project has been developed in the framework of the ELI project, born from the collaboration of 13 European countries and aims at the creation of an international laser research infrastructure that will host high level research on ultra-high intensity laser, laser-matter interaction and secondary light sources. Its goal is to reach pulse peak power and brightness beyond the current state of the art by several orders of magnitude. Because of its unique properties, this multidisciplinary facility will provide new opportunities to study the fundamental processes unfolded during light-matter interaction. ELI will be implemented as a distributed research infrastructure based initially on 3 specialized and complementary facilities (or pillars):

- **ELI Beamlines (Prague (Czech Republic))**: High Energy Beam Science pillar devoted to the development and usage of dedicated beam lines with ultra short pulses of high energy radiation and particles reaching almost the speed of light.

- **ELI Attosecond (Szeged (Hungary))**: Attosecond Laser Science pillar designed to conduct temporal investigation of electron dynamics in atoms, molecules, plasmas and solids at attosecond scale (1×10^{-18} s).

- **ELI-NP (Magurele (Romania))**: Laser-based Nuclear Physics pillar will generate radiation and particle beams with much high energy and brilliance suited to studies of nuclear and fundamental processes.

At the ELI-NP pillar, the ELI-NP-GBS is foreseen as a major component of the infrastructure, aiming at producing extreme γ-Ray beams for nuclear physics and photonics experiments characterized by unprecedented performances in terms of monochromaticity, brilliance, spectral density, tunability and polarization. The ELI-NP source [24, 26] is a machine based on the collision of an intense high power Yb:Yag J-class laser and an high brightness electron beam with a tunable energy produced by a normal conducting Linac. Referring

to Equation 2.1, this source operates at the transition between the classical and the quantum regimes: since the required bandwidth is very narrow, the quantum effects cannot be neglected. The main specifications of the Compton Source are: photon energy tunable between 0.2 and 19.5 MeV, RMS relative bandwidth lower than 0.5% and spectral density larger than 5×10^3 photons/s $*$ eV, with source spot size smaller than 100 μm and linear polarization of the γ-Ray beam larger than 95%. Moreover, the peak brilliance of the gamma beam is expected to be larger than 1×10^{19} photons/(s $*$ mm^2 $*$ mrad^2 $*$ 0 1%). To reach these challenging specifications, the luminosity L of the source must be larger than 1×10^{35} s^{-1} $*$ cm^{-2}, as specified by Equation 2.3.

$$L = \frac{N_e N_p F_r}{4\pi\sigma_0^2},$$

(2.3)

where N_p are the photons carried by the laser pulse at the collision, N_e the electrons carried in the bunch, σ_0 the spot size at the Interaction Point (IP) and F_r the repetition rate of the collisions (assuming ideal overlap in space and time of the two colliding pulses, as well as negligible diffraction of the two beams over the interaction distance). The total number of photons scattered per second, all over the spectrum and solid angle, is given by the luminosity multiplied by the total cross section $N = L\theta_{tot}$ (in ELI-NP-GBS case 7×10^{10} photons/s). Any Compton source generates polychromatic beam, hence, in order to produce a monochromatic photon beam, it is necessary to select a narrow cone around the electron beam propagation axis by means of special collimators. Therefore, what really matters for experiments and applications is the number of photons carried by the radiation pulse within a small angle N_{bw}, and their associated RMS bandwidth $\Delta\nu_p$. This is the definition of spectral density, which is the figure of merit interesting for nuclear physics and photonics applications. The Spectral Density, defined as 2.4, is typically expressed in units of photons/s $*$ eV.

$$SD = \frac{N_{bw} F_r}{\sqrt{2\pi}\Delta\nu_p}.$$

(2.4)

Various generations of machines have improved this parameter, from values of the order of 1 for bremsstrahlung sources, to about 100 for the present HiγS facility [14], towards the 10^4 range which is the goal of ELI-NP-GBS. Since

the laser pulse carries about 10^{18} photons at the IP, but only a maximum of 10^7 photons are scattered at each collision (in other words the electron beam is almost transparent to the laser pulse), the laser pulse can be "recycled" bringing it back to a new collision at the same IP with a new incoming electron bunch. To recirculate the laser pulse, an advanced and innovative laser re-circulator has been developed and it is presently under test. A full description of this new optical device can be found in [27]. To achieve this outstanding performance the laser pulse needs to be recirculated 32 times at the IP and consequently the Linac will accelerate 32 electron bunches (separated by 16.1 ns) within the same RF bucket, with a repetition rate of 100 Hz. The final parameters of the gamma beam of ELI-NP-GBS are summarized in Table 2.1 and the layout of the entire building is shown in Figure 2.2.

Table 2.1. Main parameters of the ELI-NP-GBS Gamma beam.

Energy (MeV)	0.2-19.5
Spectral Density (photon/s $* eV$)	$0.8\text{-}4 \times 10^4$
Bandwidth RMS (%)	≤ 0.5
Photons per Pulse	$\leq 2.6 \times 10^5$
Photons per Second	$\leq 8.3 \times 10^8$
RMS Size (µm)	10-30
RMS Divergence (µrad)	25-200
Peak Brilliance (photon/s $* mm^2 * mrad^2 * 0\,1\%$)	$1 \times 10^{20}\text{-}1 \times 10^{23}$
RMS Pulse Length (ps)	0.7-1.5
Linear Polarization (%)	> 99

2.3   ELI-GBS Linac Layout

In order to reach these challenging performances innovative and advanced components have been developed specifically for this machine. In order to accelerate the multi-bunch electron beam, the ELI-NP-GBS adopts an S-band (2856 MHz) photo-injector coupled to a C-band (5712 MHz) Radio-Frequency (RF) Linac capable to bring the electron beam up to an energy of 740 MeV with outstanding beam quality [28]: normalized RMS emittance in both planes below 0.5 mm $* mrad$ and energy spread below 0.1%; in Tables 2.2 and 2.3 are summarized the main required parameters of the electron beam. In order to increase as much as possible the number of collision per second, the Linac will
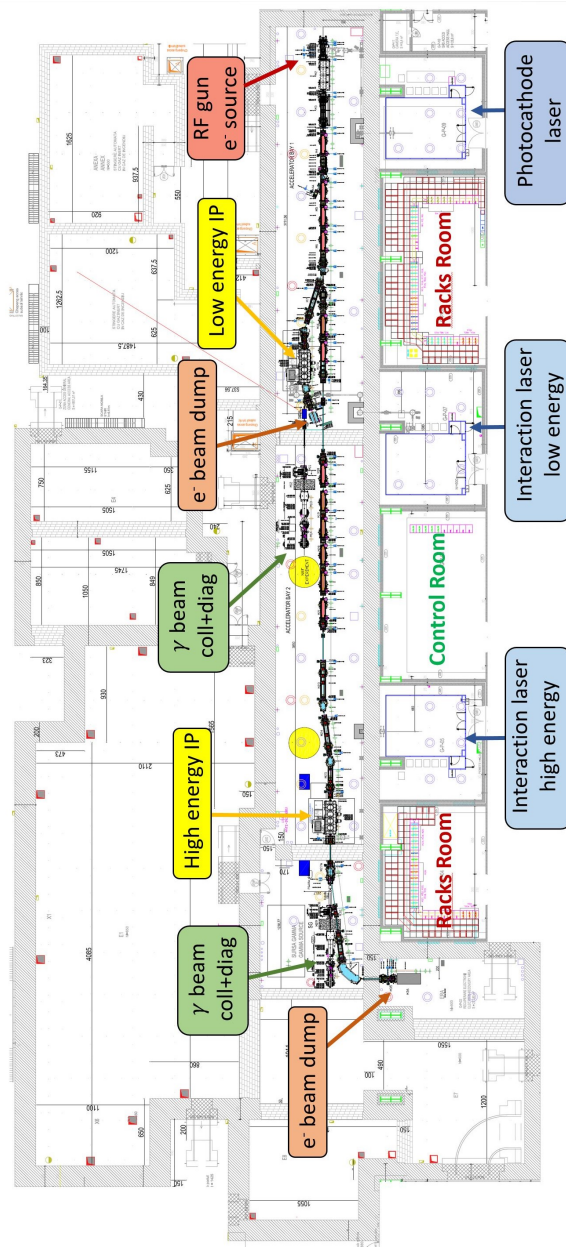
Figure 2.2. ELI-NP-GBS layout.

Table 2.2. Main parameters of the ELI-NP-GBS electron beam.

Energy (MeV)	75-740
RMS Energy Spread (%)	0.04-0.1
Bunch Charge (pC)	25-400
Bunch per Pulse	32
Bunch Separation (ns)	16.1
Bunch length (µm)	100-400
Normalized Emittance (mm $*$ mrad)	0.4
Repetition Rate (Hz)	100

work at 100 Hz repetition rate and in multi-bunch scheme; these requirements have direct impact on the design of the accelerating structures and in the overall RF system.

Table 2.3. Main parameters of the ELI-NP-GBS laser beam.

Pulse Energy (J)	0.2-0.4
Photon Energy (eV)	2.4
Wavelength (nm)	515
RMS Pulse length (ps)	1.5
Focal Spot Size w_0 (µm)	28
RMS Bandwidth	$\leq$0.1
Collision Angle (°)	172
Repetition Rate (Hz)	100
Recirculator Rate per Laser Pulse	32

To realize a reliable and compact machine a hybrid S/C-band scheme has been chosen: the combination of C-band acceleration with an S-band injector allows to obtain good performance in terms of beam quality [29]. The injector is derived from the one of SPARC_LAB Linac [30] at INFN Frascati laboratories and is composed by one 1.6 cell RF gun with copper photo-cathode and emittance compensation solenoid, followed by two SLAC-type 3 m long Travelling Wave (TW) sections To compensate space charge effect in the gun region and to reduce the bunch length, the velocity bunching technique [31] is applied in the first accelerating section placed after the gun: this technique consists in injecting a non-relativistic beam in an RF structure with a phase near the zero crossing of the acceleration field. In this way, the beam slips back up to the acceleration phase undergoing a quarter of synchrotron oscillation and is chirped and compressed; in the ELI-NP-GBS case, a compression

factor below 3 in the first accelerating section allows injecting into the C-band booster a beam that is short enough to reduce the final energy spread, avoiding also emittance degradation. In the first accelerating section, the transverse emittance dilution is controlled by a solenoid embedded to the RF compressor; the C-band booster comprises 12 TW C-band room temperature accelerating structures, downstream of the S-band photo-injector.

Two beamlines are planned to deliver the electron beam at the two Compton IPs: one at low energy ($E_e = 312\,\mathrm{MeV}$) and one at high energy (up to $740\,\mathrm{MeV}$). Downstream the injector and the first four C-band structures, a dogleg with two dipoles provide an off axis deviation towards the low energy interaction point; at the end of the Linac a second dogleg drives the beam to the high energy Compton IP. After each interaction point the electron beam is driven through dipoles towards the low and high energy dump, while the Compton radiation proceeds in straight direction towards the collimator and the γ-Ray diagnostics (Compton spectrometer, calorimeter, etc.) in the experimental rooms.

The beam characterization is essential to properly match the electron beam coming from the RF Linac to provide the required phase space orientation at the IP. The beam envelope is captured in several positions along the machine and in particular at the gun exit, at the low and high energy Linac entrance and exit and at the IPs. All the 23 monitoring positions are equipped with both a YAG:Ce and an Optical Transition Radiation (OTR) screen; the detectors are the Basler "Scout scA640-70gm" CCD camera [32]. In case of some more crucial measurements, a Hamamatsu "Orca-Flash 4" gated camera with an intensifier [33] can be used; more details on the optic system will be shown in the Chapter 4. The imaging on the screen mounted at the gun exit is used for the beam energy measurement, provided by means of the beam deflection a steerer (horizontal or vertical) upstream the screen, and to center the beam on the photo cathode. The longitudinal phase space characterization is obtained using a S-band RF deflecting cavity [34] coupled with a dipole in two main locations: downstream the first C-band cavity of the low energy Linac and upstream the first C-band cavity of the high energy Linac. The 6D phase space characterization is completed in these places with the emittance measurements by means of the quadrupole scan technique. The latter can be also done at each straight-on section of the Linac to keep under control the eventual emittance

dilution. Four beam current monitors are placed at the gun exit and all along the machine in order to optimize the beam charge transport up to the IP. The current measurements at the gun exit together with a RF injection phase scan enables the identification of the proper injection phase needed to maximize the beam energy gain as indicated by the beam dynamics simulations. The beam trajectory is measured by 29 stripline beam position monitors (BPM) all along the machine and, at the interaction region entrance and exit, by cavity BPMs which resolution is of the order of $2\,\mu m$ instead of $10\,\mu m$ of the stripline BPMs. Finally, beam loss monitors are placed all along the machine.

Chapter 3

Transition Radiation

This Chapter is a description of the theory behind the transition radiation: at first only the case of a single electron is considered and then, the case of a particle beam is treated (Section 3.3).

For the single particle case, different situations have been considered: the angle of incidence of the particle in Section 3.2.1, the distance between detector and the source of radiation in Section 3.2.2 (Far and Near Field) and the screen dimension in Section 3.2.3.

For a particle beam case, also the coherent radiation has been treated in Section 3.3.1

However, in the ELI-NP-GBS case, the radiation expected will be incoherent and in the far field; hence, in the next Chapters, only the issues related to this type of radiation will be considered.

3.1 Radiation from Moving Particles

Relativistic electrons can produce radiation if their motion is appropriately driven; the features of this radiation are linked to the particle trajectories. Considering Fig. 3.1, the general expression that gives the intensity of the radiation emitted by an electron in the direction of observation $\boldsymbol{n}$ as a function of its position, velocity and acceleration along the trajectory can be obtained from the Lienard-Wiechert field [35] and it can be written as:

$$\frac{d^2 I}{d\omega d\Omega} = \frac{e^2}{16\pi^3 \epsilon_0 c} \left| \int_{-\infty}^{+\infty} \exp[\jmath\omega(t - \boldsymbol{n} \cdot \boldsymbol{r}(t)/c)] \frac{\boldsymbol{n} \times \left[(\boldsymbol{n} - \boldsymbol{\beta}) \times \dot{\boldsymbol{\beta}}\right]}{(1 - \boldsymbol{\beta} \cdot \boldsymbol{n})^2} dt \right|^2 . \quad (3.1)$$
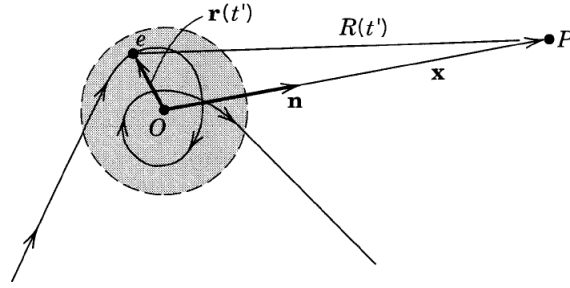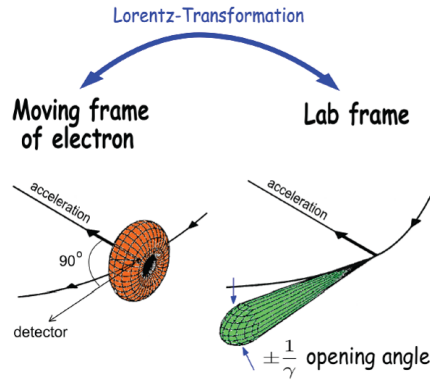
Figure 3.1. Scheme of the radiation generation for an electron with a generic trajectory $\boldsymbol{r}(t)$.

Equation 3.1 represents the energy radiated within a spectral bandwidth $d\omega$ and a solid angle $d\Omega$ centered on the direction of observation $\boldsymbol{n}$; here $\boldsymbol{r}(t)$ is the electron position at the time t, $\boldsymbol{\beta}$ is its velocity normalized to the speed of light c, $\dot{\boldsymbol{\beta}}$ is the acceleration divided by c and ϵ_0 is the vacuum permittivity. The observation point P is placed at a distance far from the electron so that the unit vector $\boldsymbol{n}$ can be considered constant along the trajectory. Equation 3.1 implies that when there is no acceleration, no radiation is emitted by the electron: hence, the acceleration is responsible for the emission of electromagnetic waves from charged particles.

Furthermore, considering the term $(1 - \boldsymbol{\beta} \cdot \boldsymbol{n})^{-2}$, the radiated energy is maximum when $\boldsymbol{\beta} \cdot \boldsymbol{n} \to 1$: this condition is verified when $\beta \approx 1$ and $\boldsymbol{\beta} \parallel \boldsymbol{n}$. Thus, a relativistic electron will radiate orders of magnitude higher than a non-relativistic one. This is the consequence of the Lorentz transformation: for an electron emitting an isotropic radiation in its rest frame, the Lorentz transformation implies that the radiation is highly collimated in a small cone of opening angle $1/\gamma$, when observed in the laboratory frame (see Fig. 3.2).

Moreover, the term $(\boldsymbol{n} - \boldsymbol{\beta}) \times \dot{\boldsymbol{\beta}}$, together with the relations between applied force and acceleration ($\dot{\boldsymbol{\beta}}_\parallel \propto \boldsymbol{F}_\parallel / \gamma^3$ for a longitudinal force and $\dot{\boldsymbol{\beta}}_\perp \propto \boldsymbol{F}_\perp / \boldsymbol{\gamma}$ for a transverse force with respect to the velocity), indicates that applying a transverse force (i.e. synchrotron radiation [37] or Free Electron Lasers [38]) is more efficient than a longitudinal one with the power that increases with the square of the acceleration [39].

Figure 3.2. Scheme of the Lorentz transformation. Picture taken from [36].
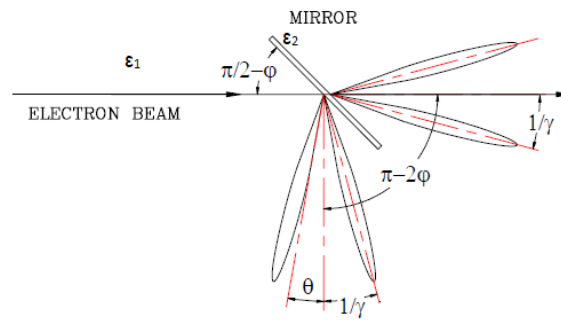
Figure 3.3. Scheme of the transition radiation generation. Picture taken from[46].

3.2 Single Particle Transition Radiation

The Transition Radiation (TR) happens when the moving particle crosses the boundary between two media with different dielectric constant. The electromagnetic field carried by the particle changes abruptly upon the transition from one medium to the other; to satisfy the boundary conditions for the electric and the magnetic field vectors, one has to add two radiation fields: one propagating in backward direction and the other in forward direction. This radiation is called transition radiation and it was first theorized by Ginzburg and Frank [40] in 1946. The analytical derivation of the equation of radiation is based on the solution of the Maxwell's equations [41]: some authors use the retarded potential method [42, 43]; other authors propose the use of the Hertz potential [44] or the image charge method [45].

At the boundary, therefore, two radiation beams are generated: one propagates in the first medium (backward transition radiation) and the other propagates in the second medium (forward TR) as shown in Fig. 3.3: solving

the Maxwell's equations one can derive the equations for the two radiations [41].

$$
\left[\frac{dI_{SP}^2(\boldsymbol{n},\omega)}{d\omega d\Omega}\right]_1 = \frac{e^2\beta^2\sqrt{\epsilon_1}\sin^2\theta_1\cos^2\theta_1}{4\pi^3 c\epsilon_0}\left|\frac{(\epsilon_2-\epsilon_1)\left(1-\beta^2\epsilon_1+\beta\sqrt{\epsilon_2-\epsilon_1\sin^2\theta_1}\right)}{(1-\beta^2\epsilon_1\cos^2\theta_1)\left(1+\beta\sqrt{\epsilon_2-\epsilon_1\sin^2\theta_1}\right)}\right|^2
$$

$$
\times\left|\frac{1}{\epsilon_2\cos\theta_1+\sqrt{\epsilon_1\epsilon_2-\epsilon_1^2\sin^2\theta_1}}\right|^2. \tag{3.2}
$$

Equation 3.2 refers to the backward radiation and Equation 3.3 refers to the forward one: the subscript indicates the medium. It is interesting to note that one equation can be obtained from the other with a permutation of the subscripts and substituting β with $-\beta$.

$$
\left[\frac{dI_{SP}^2(\boldsymbol{n},\omega)}{d\omega d\Omega}\right]_2 = \frac{e^2\beta^2\sqrt{\epsilon_2}\sin^2\theta_2\cos^2\theta_2}{4\pi^3 c\epsilon_0}\left|\frac{(\epsilon_1-\epsilon_2)\left(1-\beta^2\epsilon_2-\beta\sqrt{\epsilon_1-\epsilon_2\sin^2\theta_2}\right)}{(1-\beta^2\epsilon_2\cos^2\theta_2)\left(1-\beta\sqrt{\epsilon_1-\epsilon_1\sin^2\theta_2}\right)}\right|^2
$$

$$
\times\left|\frac{1}{\epsilon_1\cos\theta_2+\sqrt{\epsilon_1\epsilon_2-\epsilon_2^2\sin^2\theta_2}}\right|^2. \tag{3.3}
$$

It is also interesting to note that the radiation is proportional to $|\epsilon_2-\epsilon_1|^2$ and, for non relativistic particles, to the square of the velocity; in general, the dielectric constant is a function of the frequency.

In most practical case for beam diagnostics in a accelerator, the equations can be simplified: indeed, in a particle accelerator, the transition happens between vacuum and a media (i.e. aluminum) for the backward transition radiation and between a media and the vacuum for the forward radiation. In the case of relativistic particles, the Equations 3.4 and 3.5 can be reduced to [47]:

$$
\left[\frac{dI_{SP}^2(\boldsymbol{n},\omega)}{d\omega d\Omega}\right]_1 = \frac{e^2}{4\pi^3 c\epsilon_0}\frac{\sin^2\theta}{\left(\frac{1}{\gamma^2}+\sin^2\theta\right)^2}\left|\frac{\sqrt{\epsilon_2}-1}{\sqrt{\epsilon_2}+1}\right|^2, \tag{3.4}
$$

$$
\left[\frac{dI_{SP}^2(\boldsymbol{n},\omega)}{d\omega d\Omega}\right]_2 = \frac{e^2}{4\pi^3 c\epsilon_0}\frac{\sin^2\theta}{\left(\frac{1}{\gamma^2}+\sin^2\theta\right)^2}. \tag{3.5}
$$

Equation 3.4 differs from Equation 3.5 only for a term which is dependent on the dielectric constant of the medium that represents the reflectivity of

the material; furthermore, Equation 3.5 is the well known Ginzburg-Frank formula [40].
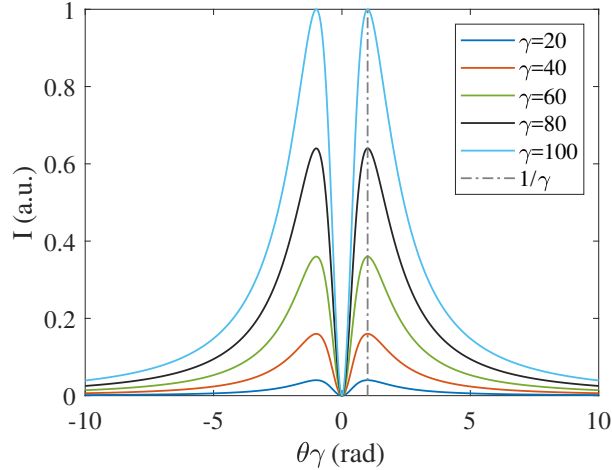
Figure 3.4. Transition Radiation for different energy: the intensities are normalized to the highest intensity value; the gray dot-dashed line represents the value $\theta_M = 1/\gamma$ where the peaks of the distributions are located. The blue line represents a γ equal to 20, the red one a γ equal to 40, the green line 60, the black one 80 and the cyan line represents a γ equal to 100. The peak of the intensity scales with the square of the energy.

In the highly relativistic regime ($\gamma \geq 20$) we can consider very small angles θ, hence we can approximate $\sin \theta$ with the angle itself: it is easy to verify that the peaks of the distribution are placed at $\theta_M = \pm 1/\gamma$ (see Figure 3.4).

3.2.1 Oblique Incidence

We have assumed thus far a normal incidence of the particle trough the surface; however, a typical use of transition radiation as a diagnostic tool requires a 45° tilt of the TR screen (see Fig. 3.3). Hence, it is important to evaluate the effect of an oblique incidence on the radiation. The issue of the radiation produced by a particle crossing an interface at oblique incidence was extensively investigated by Ashley [44] and Pafomov [48]: the derivation of the equations for the oblique incidence is rather cumbersome. In the case where one of the medium is vacuum, the equations can be written [41] as in

Equation 3.6 and 3.7:

$$\left[\frac{I_{SP}^{\parallel}(\boldsymbol{n},\omega)}{d\omega d\Omega}\right]_2 = \frac{e^2\beta_z^2\cos^2\theta_z|1-\epsilon|^2}{4\pi^3\epsilon_0 c[(1-\beta_x\cos\theta_x)^2-\beta_z^2\cos^2\theta_z]^2\sin^2\theta_z}$$

$$\times\left|\frac{(1-\beta_z\sqrt{\epsilon-\sin^2\theta_z}-\beta_z^2-\beta_x\cos\theta_x)\sin^2\theta_z+\beta_x\beta_z\cos\theta_x\sqrt{\epsilon-\sin^2\theta_z}}{(1-\beta_x\cos\theta_x-\beta\sqrt{\epsilon-\sin^2\theta_z})(\sqrt{\epsilon-\sin^2\theta_z}+\epsilon\cos\theta_z)}\right|^2,$$

$$(3.6)$$

$$\left[\frac{dI_{SP}^{\perp}(\boldsymbol{n},\omega)}{d\omega d\Omega}\right]_2 = \frac{e^2\beta_x^2\beta_z^4\cos^2\theta_y\cos^2\theta_z|1-\epsilon|^2}{4\pi^3\epsilon_0 c[(1-\beta_x\cos\theta_x)^2-\beta_z^2\cos^2\theta_z]\sin^2\theta_z}$$

$$\times\left|\frac{1}{(1-\beta_x\cos\theta_x-\beta_z\sqrt{\epsilon-\sin^2\theta_z})(\sqrt{\epsilon-\sin^2\theta_z}+\cos\theta_z)}\right|^2.$$

$$(3.7)$$

In order to obtain the backward radiation, one must permute the subscript 1 and 2 and substitute β_z with $-\beta_z$; the radiation is here decomposed in the parallel ($I^{\parallel}$) and perpendicular ($I^{\perp}$) polarizations with respect to the radiation plane (the plane defined by the photon direction and the normal to the reflecting surface). The incidence direction is determined by the values $\beta_z = \beta\cos\psi$ and $\beta_x = \beta\sin\psi$; and the direction of radiation is determined by the directing cosine of the wave vector $\boldsymbol{k}$. The directing cosine can be written as $\cos\theta_x = \sin\theta_{1,2}\cos\psi$; $\cos\theta_y = \sin\theta_{1,2}\sin\psi$; $\cos\theta_z = \cos\theta_{1,2}$.

Assuming an angle of incidence $\psi = 0$, the perpendicular component is equal to zero and the parallel one is equal to Equation 3.3 as expected (normal incidence); while, when the particle incidence is 90°, the radiation vanishes since both the parallel and the perpendicular radiation are proportional to the cosine of ψ (to the second and the fourth power of it, respectively). The main effect of the incidence angle is to break the symmetry of the two lobes of radiation (different peak value between left and right lobe) as can be seen in Figure 3.5: this effect is more visible at low energies, while for a γ equal to 100 the asymmetry is already reduced to few percent. The asymmetry in the distribution arises from the "large angle" contribution of the forward emitted radiation, that is significantly present only for directions close to the surface.
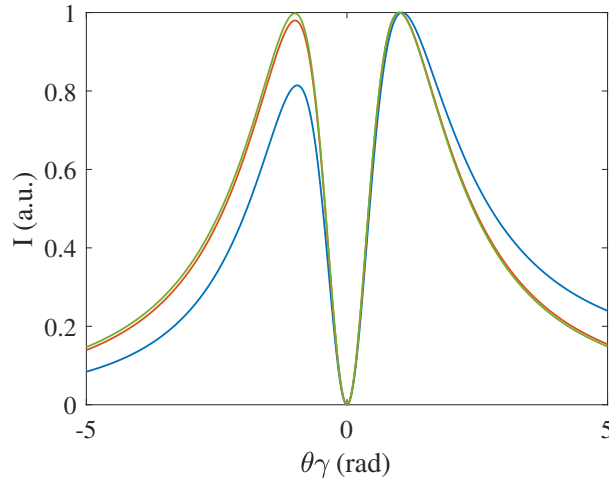
Figure 3.5. Theoretical backward transition radiation patterns at different energies of the incident electron (incidence angle of 45°). The blue curve represents an electron energy of 10 MeV; the red line represents the case of 100 MeV and the green line represents an energy of 1 GeV.

3.2.2 Near Field Regime

We assume that, as stated before, the distance between the observation point and the source of radiation must be long enough (it is the so called Far Field regime). More precisely, the distance must be much larger than the formation zone in vacuum (sometimes called also coherence length) which can be defined as the length for which the phase difference between radiation field and particle field is equal to 1 rad.

The analytical evaluation of the formation zone can be obtained using the Landau-Lifshits classical method [49]. At relativistic energies, the formation zone can be written as $\gamma^2\lambda/\pi$ with λ the observation wavelength [50].

In the ELI-NP-GBS case, with beam energies in the order of hundreds of MeV and observation wavelength in the optical spectrum, the far field regime is reached just after few millimiters; however, when the beam energy is on the order of the GeV like, for instance, at XFEL [51] where it reaches 20 GeV, the formation zone is on the order of hundreds of meters (see Figure 3.7). This means that the transition radiation diagnostics must be performed in a regime different from the far field that is called near field regime.
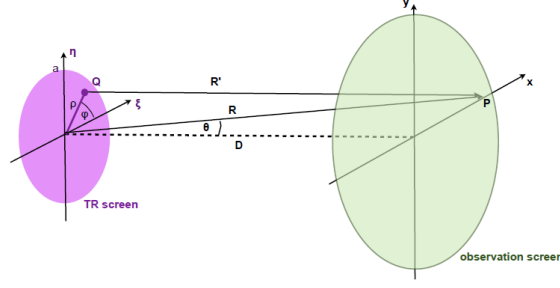
Figure 3.6. Geometry for a transition radiation screen of radius a and an observation screen placed at a distance D. Picture taken from [52].

In this regime the angular distribution can be written as in Equation 3.8:

$$
\left[\frac{dI^2_{SP}}{d\lambda d\Omega}\right]_{Near} = \frac{e^2 k^4}{4\pi^3 \epsilon_0 c \beta^4 \gamma^2} \left| \int_0^a K_1\left(\frac{k\rho}{\beta\gamma}\right) J_1(k\rho\sin\theta) \exp\left(\jmath \frac{k\rho^2}{2R}\right) \rho d\rho \right|^2,
$$
(3.8)

where $k = 2\pi/\lambda$, a is the screen transverse dimension, ρ is the radial coordinate of the source field and R is the distance from the source field [52] (see Figure 3.6). If the distance R is big enough, then the phase term in the integrand tend to unity and, assuming the transverse dimension of the screen a large enough, Equation 3.8 becomes the one of the far field regime already seen in Equation 3.5.
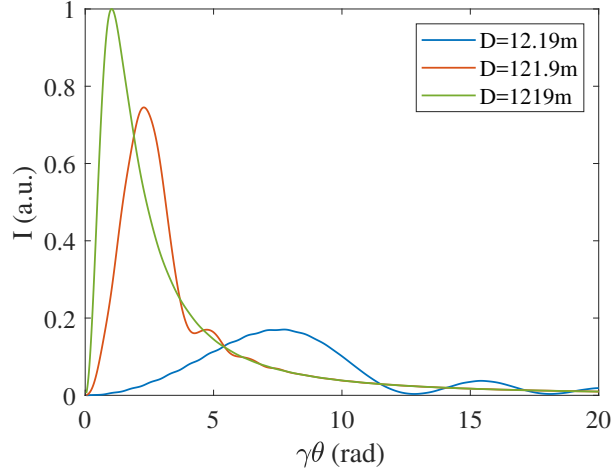
Figure 3.7. Near field optical transition radiation calculated according to Equation 3.8: the energy is $20\,\mathrm{GeV}$ (the maximum energy of XFEL) and the observation wavelength is $500\,\mathrm{nm}$. Three different distance where considered: $12.19\,\mathrm{m}$, $121.9\,\mathrm{m}$ and $1219\,\mathrm{m}$.

3.2.3 Transition Radiation from Finite Screens

Another important assumption we made is that the transition radiation screen must be infinite: under this condition the radiation can be considered a "white spectrum" (neglecting the frequency dependence of the material reflectivity); in a more realistic condition, the transverse dimension of the screen must be much bigger than the radial dimension of the particle field; otherwise, the fringe effects must be taken into account and the result is no longer frequency independent. The transverse radius of the particle field is equal to $\gamma\lambda/2\pi$: hence, at a fixed wavelength λ, the transverse dimension of the particle field is directly proportional to the energy and, at fixed energy, it is proportional to the wavelength.

Typically, for diagnostic purpose, the transition radiation is observed in the optical spectrum (OTR): considering the maximum energy expected at ELI-NP-GBS (720 MeV), the transverse dimension is about 0.2 mm while the OTR screen transverse size is 3 cm. In order to have a transverse dimension of 3 cm at a wavelength of 700 nm, instead, the energy must be 138 GeV; for higher energies, the fringe effects must be considered.

We now consider the effect of a finite screen on the radiation. For a cylindrical geometry (see Figure 3.6), it is possible to perform this analysis with the so called virtual photon method [52]: at the transition from vacuum to the surface (here assumed a perfectly conducting metal), virtual photons are converted into real photons and reflected at the interface. With this approach,
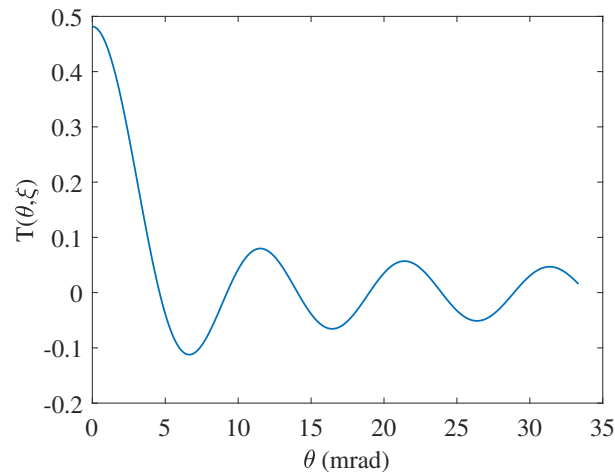
Figure 3.8. The correction factor $T(\omega, \theta)$ plotted as a function of θ. The screen radius is 3 cm, the frequency is 1 THz and γ is equal to 300.

a generalized Ginzburg-Frank equation can be written as:

$$\frac{dI_{SP}^2}{d\Omega d\lambda} = \left[\frac{dI_{SP}^2}{d\Omega d\lambda}\right]_{GF} [1 - T(\theta, \lambda)]^2, \tag{3.9}$$

$$T(\theta, \lambda) = \frac{2\pi a}{\lambda\gamma} \left[J_0 \left(\frac{2\pi a\theta}{\lambda}\right) K_1 \left(\frac{2\pi a}{\lambda\gamma}\right) + \frac{J_1 \left(\frac{2\pi a\theta}{\lambda}\right) K_0 \left(\frac{2\pi a}{\lambda\gamma}\right)}{\gamma\theta} \right], \tag{3.10}$$

where the term $\left[\frac{dI_{SP}^2}{d\Omega d\lambda}\right]_{GF}$ is the classical Ginzburg-Frank formula reported in 3.5. The generalized Ginzburg-Frank formula is now frequency dependent as can be seen in Figure 3.9; the variation with the frequency is introduced by the correction factor $T(\theta, \lambda)$ expressed in Equation 3.10. The correction factor is dependent on the ratio between the screen radius a and the wavelength of observation. It can be verified that for $a \to \infty$ the correction factor goes to zero and Equation 3.9 turn back into the classical Ginzburg-Frank formula; while if $a \to 0$, then the correction factor goes to 1 and no radiation is generated. An example of a plot of the correction factor is showed in Figure 3.8 for a frequency of 1 THz a screen radius of 3 cm and an energy of about 150 MeV.
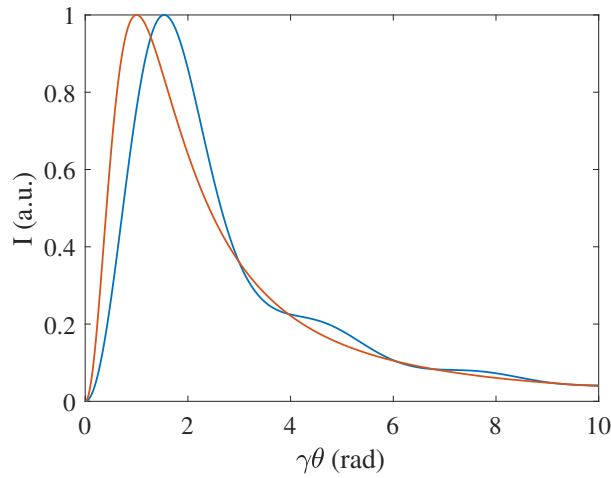
Figure 3.9. Transition Radiation curve according to Equation 3.9 for a γ equal to 100 and two different frequency: a 1 THz radiation in the blue line and a 560 THz radiation (green light) in the red line.

3.3 Transition Radiation from a Beam

In the previous sections, only the radiation produced by a single electron was considered; however, in a real measurement, a complete beam with its

6D distribution (transverse and longitudinal phase-space) must be taken into account. The total spectral angular intensity can be written as:

$$\frac{dI_{tot}^2}{d\lambda d\Omega} = \frac{dI_{SP}^2}{d\lambda d\Omega} \left\{ N + N(N-1) \left| \int \int n(\rho, z) \exp\left[\jmath\frac{2\pi}{\lambda}(z + \rho\sin\theta) \right] d\rho dz \right|^2 \right\},$$
(3.11)

where ρ and z are respectively the radial and the longitudinal positions of the N particles of the beam; $\frac{dI_{SP}^2}{d\lambda d\Omega}$ is the Single Particle Function and it is equal to the Ginzburg-Frank formula of Equation 3.5 since we are assuming a normal incidence in a perfectly conducting metal. The function $n(\rho, z)$ represents the charges distribution normalized to unity [53]. The first addendum represents the incoherent radiation and it is linearly dependent on the beam charge; the second addendum is the coherent radiation that grows quadratically with the charge. However, in the optical spectrum with a beam with longitudinal dimension σ_z of mm, the integral (called form factor) tend to zero and only the incoherent radiation can be taken into consideration: this is related to the ratio between the beam length and the wavelength.
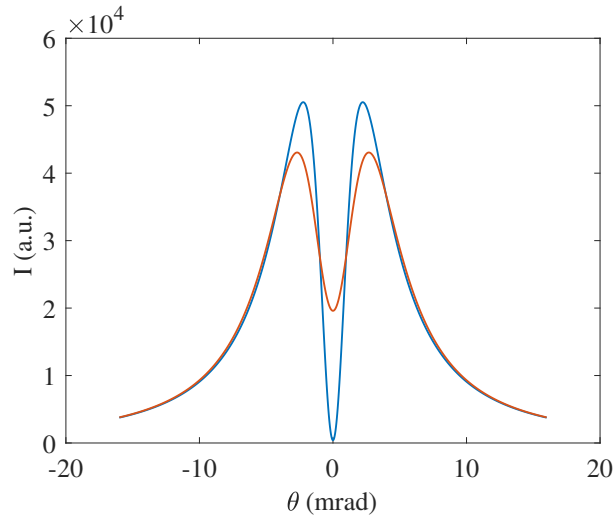
Figure 3.10. Transition Radiation for a 234 MeV energy and two different values of divergence: 0.1 mrad in the blue line and a 1 mrad in the red line.

In the case of beam, with energy spread and divergence, the first addendum of Equation 3.11 must be rewritten as a summation:

$$\frac{dI_{tot}^2}{d\lambda d\Omega} \propto \sum_{i=1}^{N} \frac{(\theta - \sigma_i')^2}{\frac{1}{\gamma_i^2} + (\theta - \sigma_i')^2}$$
(3.12)

where σ' is the particle transverse momentum. The effect of the energy spread is very weak and becomes appreciable only with values of tens of percents. Hence, neglecting the energy spread, Equation 3.12 becomes the convolution of the single particle function with the beam divergence distribution. If we can assume a Gaussian distribution of the divergences, the OTR angular distribution can be written as:

$$I = \frac{e^2}{4\pi^3 c\epsilon_0} \frac{\sqrt{\pi}\mu}{\nu} \Re\left[\Phi(z)\left(\frac{1}{2} + \mu\nu z\right)\right] - \mu^2,$$
$$\mu = \frac{1}{\sqrt{2}\sigma'}, \quad \Phi(z) = \frac{1 - \operatorname{erf}(z)}{\exp\left[-z^2\right]},$$
$$z = \mu(\nu + i\theta), \quad \nu = \frac{1}{\gamma}, \tag{3.13}$$

where $\operatorname{erf}(z)$ is the complex error function and $\Re$ is the real part [54]. Assuming a Gaussian distribution of the particle transverse momentum is reasonable in most of the cases; however, where there are strong correlations between position and angle, or between horizontal and vertical planes, or in general when the distribution is not anymore Gaussian this treatment cannot be apply and a reasonable guess of such a distribution must be considered.

Due to the beam divergence, the angular distribution of the whole beam will be different from 0 at the center (see Figure 3.10): the ratio between the minimum and the maximum intensity is related to the beam divergence. A parameter called visibility can be defined as:

$$V = \frac{I_{max} - I_{min}}{I_{max} + I_{min}}. \tag{3.14}$$

In analogy with the contrast function, the measurement with the OTR angular distribution can be reliably done if the visibility parameter is greater or equal to 0.1 [55]. I_{max} and I_{min} depends on both divergence and energy of the beam. Equation 3.14, therefore, implicitly gives the range of beam energy and divergence over which this technique can be used: since for bigger energies the angular distribution narrows, the sensitivity to angular spread is higher than for low energy beams where the angular distribution is wide as it can be seen in Figure 3.11.
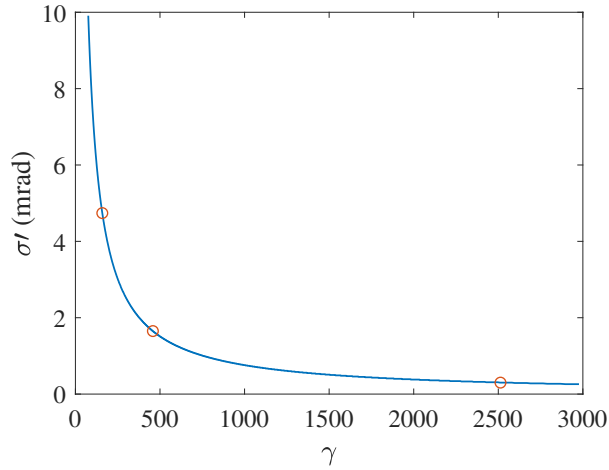
Figure 3.11. Values of divergence that corresponds to a visibility of 0.1 as a function of the energy. The red circles represent some examples of beam energy and divergence: for a beam energy of 80 MeV, the divergence must be below 5 mrad; for a beam energy of 234 MeV, the divergence must be below 2 mrad, while for a beam energy of 1.5 GeV, the divergence must be below 0.3 mrad.

3.3.1 Coherent Optical Transition Radiation

If we go back to Equation 3.11, assuming the radial and the longitudinal positions completely uncorrelated, we can factorize the charge distribution as $n(z, \rho) = \zeta(z)\tau(\rho)$: hence, the form factor can be decomposed in a longitudinal form factor $F_\parallel(\lambda)$ and a transverse form factor $F_\perp(\lambda, \theta)$. Assuming a Gaussian distributed beam for both the transverse and the longitudinal directions, the form factors can be calculated analytically [53] as:

$$F_\parallel(\lambda) = \exp\left[-\left(\frac{2\pi\sigma_z}{\lambda}\right)^2\right],$$

$$F_\perp(\lambda, \theta) = \exp\left[-\left(\frac{2\pi\sin\theta}{\lambda}\right)^2 \left(\sigma_x^2\cos^2\psi + \sigma_y^2\sin^2\psi\right)\right], \qquad (3.15)$$

where $\sigma_{x,y}$ are the horizontal and vertical RMS beam size, σ_z is the RMS bunch length and ψ is the azimuthal angle of the radiation plane. Since for an uncompressed bunch in a conventional accelerator (bunch length in the order of mm) $\sigma_z >> \lambda$ in the optical range, the form factor is ≈ 0 and only the incoherent part of the radiation is significant. The longitudinal form factor is strongly enhanced in case of a beam that is longitudinally compressed or in the presence of micro-bunching modulation [56, 57]. On the other hand, the

transverse form factor is responsible of an angular distribution narrower and less intense as the transverse beam size increase.

Due to the quadratic dependence with the charge, coherent radiation could disturb or even mask completely the measurement of the incoherent angular distribution; some authors [58] propose to image the beam in the ultraviolet spectrum to avoid the coherence radiation disturbs. On the other hand, the coherent radiation has been used as a tool to retrieve the longitudinal information of the beam [59] or as a source of THz radiation [60].

Chapter 4

Design Issue

As it was shown in the Chapter 3, the Transition Radiation happens when a charged particle crosses the boundary between two media with different electrical properties (i.e. different dielectric constant). However, depending on its charge, the particle beam may deposit not negligible amounts of energy in the target material due to this interaction. This phenomenon could determine a temperature increase that may deform the OTR target surface; this deformation may influence the photon emission and the diagnostics quality.

This chapter presents a study on the thermal behavior of the OTR screen (Section 4.1), using as target material aluminum and silicon [1, 61].

Similar studies have been done at the CLIC Test Facility [62], at TTF2 [63], at ATF [64] and at CEBAF [65]. Many authors propose, in case of high charge and high repetition rate, the use of graphite target (CLIC), carbon foil (CEBAF) or Beryllium target (ATF): however, in the ELI-NP-GBS case, the resolution needed imposes a planarity requirement of the screen surface that those materials do not fit. At LCLS-II [66], instead, they will use only wire scanner for the high quality transverse diagnostic, and the OTR screen will be used only in the low repetition rate diagnostic line (120 Hz while the main beam line work at 1 MHz). Table 4.1 summarizes the main beam parameters of the above mentioned machine. However, it will be shown that the thermal stress induced by the ELI-NP-GBS beam is not as high as for the CLIC and ATF case, hence a silicon screen is a good candidate.

This study has been validated by a numerical study with ANSYS simulation (Section 4.2); ANSYS was also used for the evaluation of the mean lifetime of the studied materials and to evaluate the shape and the amplitude of the

Table 4.1. Beam parameters for different machines.

	TTF2	CLIC	ATF	CEBAF	ELI-NP-GBS
Integrated Beam Charge (nC)	1	2272	3	200 µA	8
Beam Spot size (µm)	100	250	15	100	72
Beam Energy (GeV)	0.13	0.38	1.3	3.2	0.14
Pulse Rep. Rate (Hz)	10	50	1.5	CW	100

generated deformations [67, 2]. Indeed, at ATF [64], a screen damage has been experimentally observed even in the beryllium target in an extreme condition (20 µm × 12 µm transverse spot size and about 9 nC of charge of the beam pulse train).

The deformations obtained with ANSYS were implemented in the ZEMAX Optics Studio software to estimate their effects on the overall optical performances (Section 4.4). A typical OTR screen is a plate 400 µm thick with a square planar surface of 3 cm × 3 cm size.

Finally, an overall characterization of the main diagnostic stations has been shown in Section 4.5; this characterization was done in terms of magnification, resolution and number of collected photons [68, 3, 69].

4.1 Thermal Analysis

Table 4.2. Material property of aluminum and silicon [70].

		Al	Si
Specific heat ($J * kg^{-1} * K^{-1}$)	c_p	890	700
Density ($kg * m^{-3}$)	ρ	2700	2330
Melting temperature (K)	T_{melt}	933	1687
Thickness (µm)	Δz	0.05	380
Emissivity	ε	0.18	0.67
Thermal Conductivity ($W * m^{-1} * K^{-1}$)	k	209	143.5
Thermal Diffusivity ($m^2 * s^{-1}$)	α_d	8.418×10^{-5}	8.8×10^{-5}
Tensile Strength (MPa)	σ_{ten}	110	225
Coeff. Thermal lin. expansion (K^{-1})	α_t	23×10^{-6}	2.5×10^{-6}
Young's Modulus (GPa)	E_y	69	150
Electron Stopping Power ($J * m^{-1}$)	$\partial E/\partial z$	8.65×10^{-11}	7.47×10^{-11}

When a single particle hits a surface, it deposits an amount of energy ΔE

according to:

$$\Delta E = \frac{\partial E}{\partial z} \rho \Delta z, \tag{4.1}$$

where ρ is the density of the material and Δz is its thickness; the electron stopping power $\partial E / \partial z$ depends on the material and on the particle energy while, here, it can be considered spatially independent. Often, in literature, the mass stopping power, which is obtained by dividing the electron stopping power by the density material, is instead used: in this way, the value is material independent. Typical values used for the energy of interest are $2\,\mathrm{MeV} * \mathrm{cm}^2 * \mathrm{g}^{-1}$ [62] or $1.61\,\mathrm{MeV} * \mathrm{cm}^2 * \mathrm{g}^{-1}$ [63] or $1.64\,\mathrm{MeV} * \mathrm{cm}^2 * \mathrm{g}^{-1}$ [71]; For all the calculation showed in this work, the values in Table 4.2 has been used: this gives a mass stopping power of $2\,\mathrm{MeV} * \mathrm{cm}^2 * \mathrm{g}^{-1}$.

Assuming an electron beam with a Gaussian spatial distribution hitting the surface, the target temperature $T(x, y, t)$ obeys to the equation [72]:

$$\frac{\partial T(x, y, t)}{\partial t} = \frac{1}{c_p \rho} \left\{ \frac{\partial E}{\partial z} \frac{N_e(t) \rho}{2\pi \sigma_x \sigma_y} \exp\left(-\frac{x^2}{2\sigma_x^2} - \frac{y^2}{2\sigma_y^2} \right) + \right.$$
$$\left. k\nabla^2 T(x, y, t) - \frac{2\epsilon \sigma_{sb}}{\Delta z} \left[T(x, y, t)^4 - T_0^4 \right] \right\}, \tag{4.2}$$

where x and y are the transverse position of the beam, σ_x (σ_y) represents the transverse beam size, c_p is the specific heat, $N_e(t)$ is the number of particle of the beam, k is the thermal conductivity, ϵ is the emissivity and σ_{sb} is the Stephan-Boltzmann constant. The first addendum represents the temperature rising, the second one is the cooling by conduction and the third one is the radiation cooling, while, since the target is in vacuum, there is not convection cooling.

When a bunch hits the screen, the temperature rises according to [62]:

$$T(x, y) - T_0 = \frac{\partial E}{\partial z} \frac{N_e}{2\pi \sigma_x \sigma_y c_p} \exp\left(-\frac{x^2}{2\sigma_x^2} - \frac{y^2}{2\sigma_y^2} \right). \tag{4.3}$$

The temperature rising depends linearly on the bunch charge and inversely on the specific heat and the dimensions of the beam, while, here, it is independent from the thickness of the screen. Therefore, a more focused beam causes more heating, as it can be seen from the Figure 4.1 which refers to a single bunch pulse. Table 4.3 shows the instantaneous temperature rise for the ELI-NP-GBS beam which is composed by 32 bunches with a charge of $250\,\mathrm{pC}$ each; the

(a)   (b)
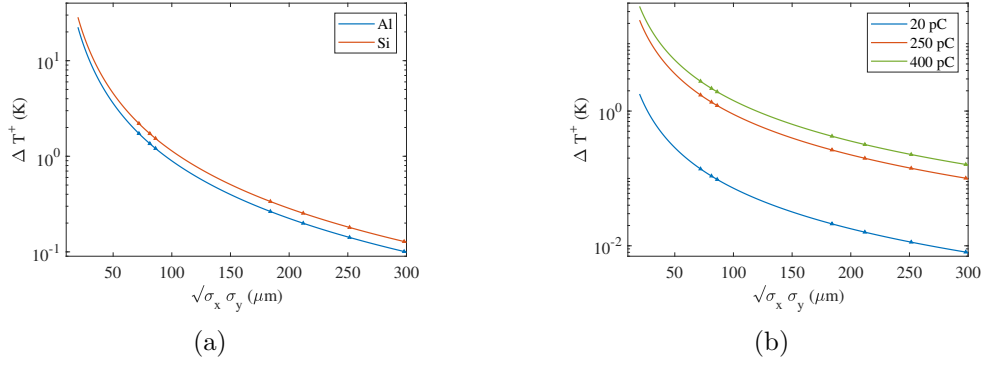
Figure 4.1. Instantaneous temperature rising as a function of the beam dimensions
for two different material (aluminum and silicon) and a bunch charge of $250\,pC$
(a). Figure (b) represents the case of an aluminum screen and three different
bunch charges ($20\,pC$, $250\,pC$ and $400\,pC$). The triangles represent the values
at the position of the OTR diagnostic stations in the ELI-NP-GBS Linac (see
Table 4.3).

spot sizes are the one estimated by beam dynamic simulations at the OTR
diagnostic stations. When the beam spot size is $47.5\,\mu m \times 109\,\mu m$ (the beam
with higher charge density), the temperature increase is higher: therefore, this
case will be studied in more details.

Table 4.3. Instantaneous temperature increase for a 32 bunches train with a charge
of $250\,pC$ each at the position of the OTR diagnostic stations in the ELI-NP-GBS
Linac. The beam with the higher charge density has been emphasized in bold
character: it causes the higher temperature increase, hence it will be studied in
more details.

$\sigma_x(\sigma_y)(\mu m)$	ΔT^+ **Al** (K)	ΔT^+ **Si** (K)
298 (298)	3	4
251 (252)	5	6
211 (213)	6	8
184 (184)	8	11
47.5 (109)	**55**	**70**
241 (27.4)	43	55
106 (70)	39	49

For the ELI-NP-GBS case, the temperature increase stays well below few
hundreds of Kelvin: hence, the radiative cooling can be considered negligible
since it becomes relevant for temperature above $1000\,K$. Therefore, it must be
taken into account only the conduction cooling. Typically, "cooling mechanism"

refers to techniques used to dissipate heat from a material (i.e. water cooling), however similar schemes are not implemented for the beam profile monitors in the machine; hence, in this thesis, the term "cooling mechanism" refers to the heat diffusion from the area of the screen that is hit by the beam to the other part of the screen and the neighborhood support frame. Since the bunch separation in the ELI-NP-GBS is 16.1 ns, the cooling intervening in the period between two bunches can be neglected; only the cooling between macro-pulses (10 ms spaced) is relevant.

The two dimensional heat conduction equation becomes [63]:

$$\frac{\partial T}{\partial t} = \alpha_d \nabla^2 T + \frac{1}{\rho c_p} q(x, y, t), \qquad \alpha_d = \frac{k}{\rho c_p}, \tag{4.4}$$

where α_d is the thermal diffusivity. The temperature of the flange can be considered independent on the temperature of the heated area and equal to the machine temperature ($T_0 = 295.15$ K); the density of the internal heat source $q(x, y, t)$ has a Gaussian form (as a function of x and y) during the passage of the electron bunch through the material slab [63]. The solution of Equation 4.4 with these assumptions therefore is:

$$\Delta T(x, y, t) = \frac{\sigma_x}{\sqrt{2\alpha_d t + \sigma_x^2}} \frac{\sigma_y}{\sqrt{2\alpha_d t + \sigma_y^2}} \Delta T(0, 0, 0) \times$$

$$\exp\left(-\frac{x^2}{2(2\alpha_d t + \sigma_x^2)} - \frac{y^2}{2(2\alpha_d t + \sigma_y^2)}\right), \tag{4.5}$$

which allows also to estimate the time needed to cool down. For the ELI-NP-GBS case, both in the case of aluminum and silicon target material, using the corresponding parameters in Table 4.2 and the spot size emphasized in 4.3, a relevant result comes out: the screen does not completely cool down after the pulse (10 ms). The interval between two pulses is not sufficient to dissipate the heat that the beam deposits, determining a general increase of the target temperature after each pulse. The resulting temperature is Gaussian-shaped with the peak in the middle of the target ($x, y = 0$). However, in just few cycles, a thermal equilibrium between the deposited and the dissipated heat is reached; at the equilibrium, the Gaussian temperature field oscillates with a period equal to the sum of the pulse length and the pulse distance, and the peak temperature oscillates between a maximum (T_{max}) and a minimum
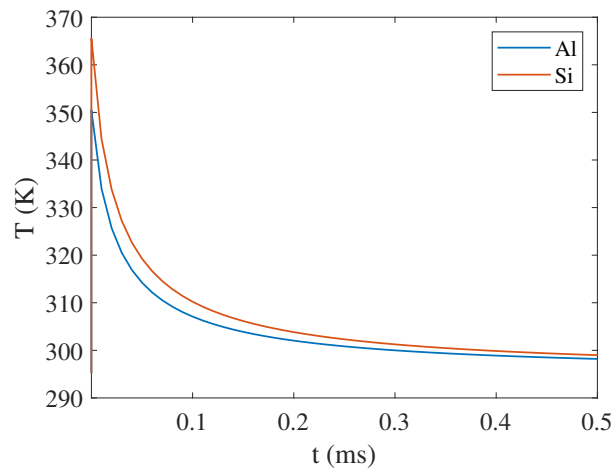
Figure 4.2. Temporal evolution of the conduction cooling after the heating of a ELI-NP-GBS bunch train (σ_x =47.5 μm, σ_y =109 μm). The values refer to the center of the impact area of the beam to the target $(x, y = 0)$.

(T_{min}) value ("steady-state oscillation"). Figure 4.2 and Figure 4.3 show that after three cycles, an equilibrium is reached: the minimum temperatures are 295.3 K for the aluminum and 295.4 K for the silicon, while the maximum ones are 350.6 K for the aluminum and 365.8 K for the silicon.
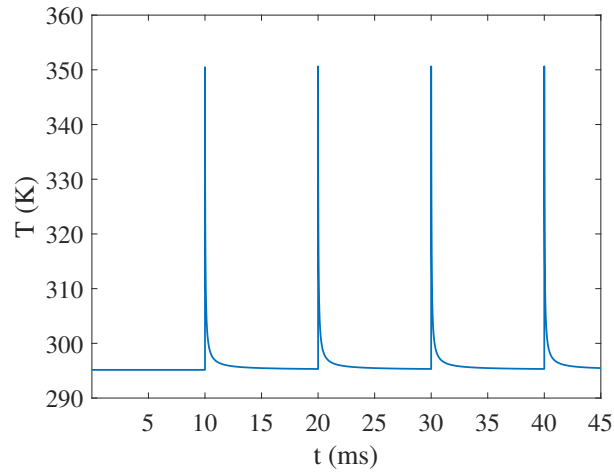
Figure 4.3. Temporal evolution of the heated area during 4 cycles of ELI-NP-GBS machine operation with a bunch train of σ_x =47.5 μm and σ_y =109 μm. The values refer to the center of the impact area of the beam to the aluminum target $(x, y = 0)$.

4.2   ANSYS Numerical Analysis

As explained in Section 4.3, the impact of the electron beam on the OTR screen, produces a continuous oscillating change of temperature of the material. The theoretical approach suggests that the oscillations reach an equilibrium condition after few cycles. The thermal simulation has been performed in ANSYS environment to validate the theory and to assess the temperature distribution over the time. Several thermal transient analysis has been performed with a dedicate ANSYS analysis.

The study of localized heating and of the cooling of the OTR target ("thermal cycle") requires the simulation of high number of impacts of the electrons. In light of this, the energy deposited by the beam is provided to the 3D mesh elements corresponding to the OTR target portion significantly interacting with the electron beam ("hotspot").

A non uniform mesh was used and it was refined close to the hotspot where the heat generation is concentrated (minimum mesh size of $6\,\mu m$). Regarding the boundary condition, it was considered an initial temperature T_0 of $295.15\,K$, corresponding to the ELI-NP-GBS machine temperature. This temperature was fixed along the edges in contact with the frame support and the screws.

The analysis introduces an approximation for the simulation of the deposited energy distribution: indeed, it associates to each entire mesh element a value calculated with the coordinates of its centroid and the electron beam properties. However, a comparison between data obtained with the analytical formula and those extracted from ANSYS simulations confirms the goodness of the approximation.

Results of the thermal transient analysis are reported in Figure 4.4. It was also used a uniform thermal power distribution: in this case, the script associates to all the nodes within the elliptic beam section the temperature given by Equation 4.3 for $x = y = 0$ ($350\,K$), and the machine temperature to the remaining nodes). Silicon presents a much more pronounced increase of temperature in the interaction area, with respect to the aluminum: this is a reasonable result taking into account the higher specific heat capacity and density of the aluminum with respect to the silicon for the same deposited electron beam energy. Aluminum reaches a steady-state maximum peak temperature of $345.3\,K$ after about 80 thermal cycles, while silicon reaches
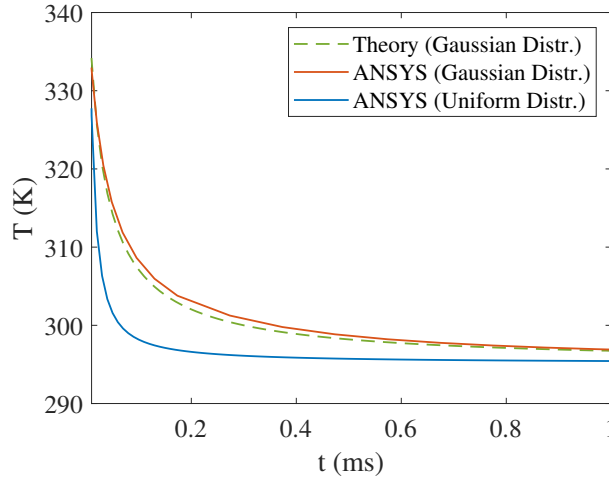
Figure 4.4. Ansys analysis of the thermal transient behavior of a given node for nominal ELI-NP-GBS (aluminum bulk screen).

the steady-state temperature of 358.9 K after about 92 thermal cycles. The difference between the two steady-state temperatures is due to the different specific heat capacity of the materials.

4.3 Thermal Stress Evaluation

Due to beam energy deposition on the OTR targets, it is expected an instantaneous temperature increase of 55 K for the aluminum and of 70 K for the silicon in the worst case scenario (higher beam charge density). The maximum instantaneous increase of temperature sustainable by a material (thermal stress limit) is given by [63]:

$$\Delta T_{stress} \approx \frac{2\sigma_{ten}}{\alpha_t E_y}, \tag{4.6}$$

where σ_{ten} is the ultimate tensile strength, σ_{sb} is the coefficient of thermal linear expansion and E_y is the Young's Modulus. From Equation 4.6 it follows that the maximum instantaneous temperature increase is 130 K for the aluminum and 1200 K for the silicon; these limits are not exceeded in nominal operation.

Nevertheless, the number of load cycles, the stress range and the occurrence of local stress concentration may still induce fatigue damages. Structural linear analysis of the OTR screen starts from results of thermal transient simulations of the two materials. Thermal distribution, determined for the hotspot at

maximum temperature, has been assigned to each node of the mesh to perform the evaluation of the OTR stress and strain. Table 4.4 reports the maximum

Table 4.4. Von Mises Stress and maximum displacement calculated by mean of ANSYS simulation for the aluminum and the silicon in the case of a beam spot size of $47.5\,\mu m \times 109\,\mu m$.

	Al	Si
Max. Von Mises Stress (MPa)	53.9	12.02
Min. Von Mises Stress (MPa)	0.13	0.04
Max. Displacement (nm)	148.5	15.9

and minimum equivalent Von Mises stress [73] for aluminum and silicon relative to number of thermal cycles that lead to material damage. The maximum stress, for both materials, is located in correspondence of the central element of the hotspot mesh, where there is the hottest point of the OTR. In Table 4.4
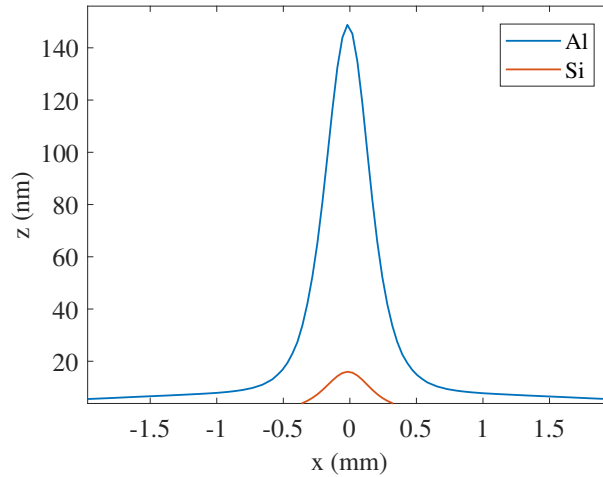
Figure 4.5. Displacement produced by the heating of the aluminum (blue curve) and the silicon (red curve) OTR screen.

and Figure 4.5, it is also reported the maximum displacement produced by the heating of the OTR screen along x and y axis of the surface. Despite the greater increase of temperature, it is evident that the silicon has a smaller deformation, thus less influence on optical properties. In this particular case, it has been obtained for the silicon a maximum displacement of $15.9\,nm$, about one order of magnitude lower than the aluminum. Even if the silicon reaches higher temperatures in the oscillation than the aluminum, its mechanical properties (e.g. higher Young's modulus) determines a better behavior in

terms of deformation that reflects in better optical quality of the screen and, thus, of the whole diagnostic system.

The equivalent Von Mises stress (σ_{VM}), obtained in the structural analysis (Table 4.4), has been used to estimate alternating (σ_a) and mean (σ_m) stress intensity:

$$\sigma_a = \frac{\sigma_{VMmax} - \sigma_{VMmin}}{2},$$
$$\sigma_m = \frac{\sigma_{VMmax} + \sigma_{VMmin}}{2}. \tag{4.7}$$

Consequently, to quantify the interaction of mean and alternating stresses, it has been applied the Goodman relation:

$$\frac{\sigma_a}{\sigma_N} + \frac{\sigma_m}{\sigma_{ten}} = 1, \tag{4.8}$$

where σ_N is the Goodman alternate stress level [73]. The Goodman relation describes the decreasing of the material lifetime with an increase of mean stress level for a given level of alternating stress. After that, the Goodman alternate stress has been used to calculate the number of cycles to failure (N) by mean of the specific S-N Wohler curve for each material [74, 75].

(a)　　　　　　　　　　(b)
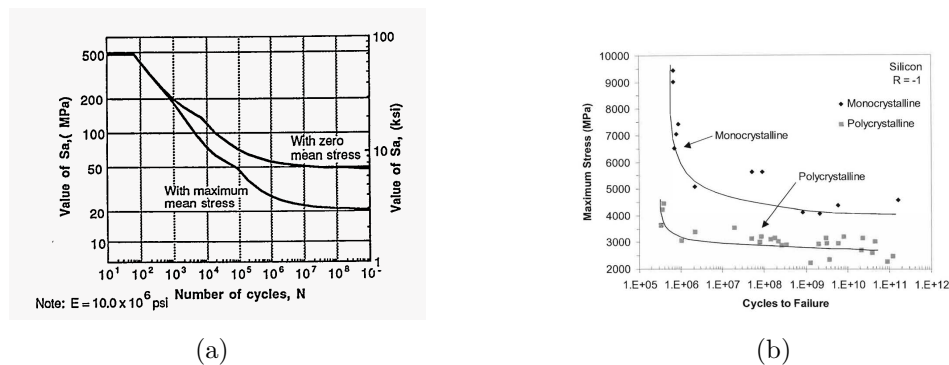
Figure 4.6. Fatigue design curve for the aluminum alloy [74] (a) and the silicon [75] (b). Considering the stress value calculated for the ELI-NP-GBS working point operations, the issues arise only for the aluminum alloy.

Aluminum reaches a Goodman alternate stress of 30.2 MPa while the silicon of 7.74 MPa: taking into account the specific S-N Wohler curves (see Figure 4.6) for the two materials, the number of cycles (N_i) which causes failure is 609 700 (less than 2 h with a 100 Hz repetition rate) for the aluminum, while it can not be estimated for the silicon.

Table 4.5. Effects of the multibunching on the thermal and the mechanical parameter of the aluminum.

# Bunches	Max. Temp. (K)	σ_a (MPa)	MTBF (h)
32	344.4	30.2	< 2
16	320.2	13.93	∞
8	307.7	6.99	∞

On the other hand, changing the characteristics of electron beam, i.e. decreasing the number of bunches, the fatigue life for aluminum increases: the rising of maximum temperature and thus mechanical stresses, are inversely proportional to the bunches' number (Table 4.5). For example, with 16 bunches instead of 32, also aluminum has no fatigue life limit just like silicon.

4.4 Optical System Simulation

A high distortion of the OTR screen surface close to the electron beam hotspot could generate a loss of image resolution [64]. For a generic monocrystalline silicon plate, the production mean square roughness is under 1 nm; therefore, the evaluation of the OTR screen strain surface is relevant for its optical performance. The prediction of the optical performances is typically done with commercially available optical design software such as ZEMAX [76] or CODEV; these softwares allow to represent surface errors and displacements by means of polynomial surface definition, surface interferogram files or uniform array of data.

The surface errors are defined by means of surface normal or sag displacement: the sag displacement is defined as the distance from the vertex tangent plane to the optical surface. ZEMAX implements the data array with the so called "Grid Sag Surface": it is a uniform array of sag displacement and/or slope data used to define a perturbation to a base surface (in our case a planar surface).

ZEMAX offers different ways to evaluate the performances of an optic system: the main ones are the geometric RMS spot size diameter and the Physical Optic Propagation Mode (POP). In the first case, a simple geometrical ray tracing analysis is performed assuming an object at infinity and three different wavelengths (486 nm, 588 nm, 656 nm): this method, however, is not

reliable in some application like, for instance, when the system is close to the diffraction limit. A more precise analysis can be done with the POP mode which take into account also diffraction and polarization of light.

The photons are reflected by a deformed mirror and then they are collected by an optical system to perform the imaging of the source. A Gaussian beam with the same spot size as the electron beam under study (see the bold line in Table 4.3) has been propagated through the optic system; the mirror deformation has been defined in accordance with the displacement created by the beam on the aluminum target and on the silicon target (149 nm and 16 nm respectively, as can be seen in Table 4.4).
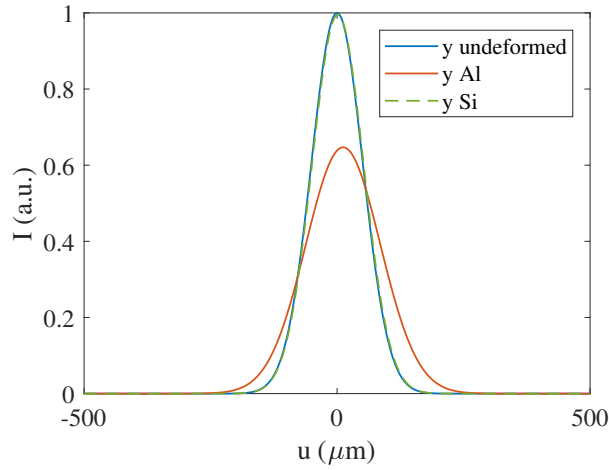
Figure 4.7. Vertical profile of a beam reflected by a mirror in the perfectly planar case (blue continuous line) and in the case of an aluminum deformation (red continuous line) and a silicon deformation (green dashed line).

The deformation causes a small translation of the centroids of the beam (below 1.4 µm for the silicon case and below 10 µm for the aluminum case); it also causes a loss of the collected photons which is negligible for the silicon case (0.4%) while it goes up to 30% for the aluminum case. A bigger issue is related to the Gaussian reconstruction of the beam in the case of the aluminum: it is negligible for the horizontal plane (47.5 µm) while is 44% in the vertical plane (109 µm), as can be seen in Figure 4.7.

This dependence of the error on the spot size is confirmed also by other simulations for different beam size: for instance, a 27 µm symmetric beam get deformed by a factor lesser than 0.01. Also the centroids and the amplitude are less affected by the displacement; furthermore, the effect is more significant on the vertical plane, where the deformation of the screen is larger. The reason

is related to the area of displacement where the beam is reflected: a bigger beam is reflected by a larger area of the deformed mirror. Indeed, the larger beam "sees" a bigger portion of the displacement.

These results show that the optical properties of the silicon screen do not change significantly even after the thermal deformation, while the ones of the aluminum screen are heavily compromised. As a result of these studies, a silicon OTR screen has been chosen for the diagnostic station; furthermore, in order to reduce the loss of optical performance and to obtain an easier lithography process of the OTR surface for the image calibration (as it will be explain next), the silicon used to produce the electrical chip has been chosen (monochristalline silicon wafer): the main characteristic is indeed the good planarity of the surface.

4.5 Resolution

The expected RMS beam size along the LINAC, provided by preliminary beam dynamics simulation, will vary in the $30\,\mu m$ - $1000\,\mu m$ range [77] (as reported in Figure 4.8). An evaluation has been done in order to find the best lenses setup that fits the requirements in term of resolution and magnification for each diagnostic station.
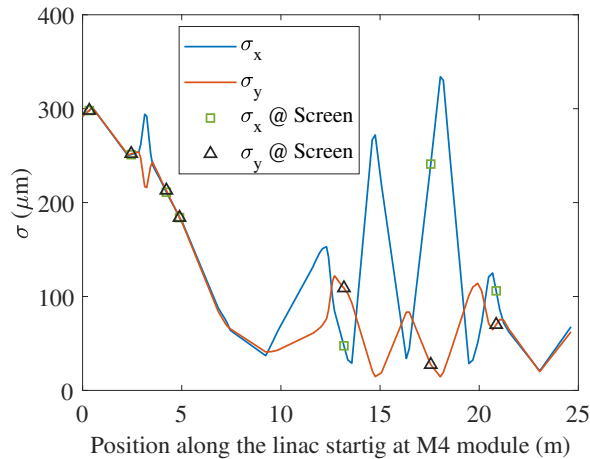
Figure 4.8. Spot size of the beam in the low energy line after the S-band photoinjector [77].

The optical acquisition system is constituted by the CCD camera "Basler scout A640-70gm" with a macro lens. A movable slide is used to place the

lens plus camera system closer or farer from the OTR target; such distance is between 60 cm and 130 cm from the OTR target due to mechanical and geometrical constraints. In order to avoid possible damage of the optics devices due to the radiation emitted by the beam, a 45° mirror is placed at 40 cm from the target leading to a minimum distance achievable of 60 cm; since the beam pipe is placed 1.5 m from the floor, the maximum distance is instead 130 cm.

(a)   (b)
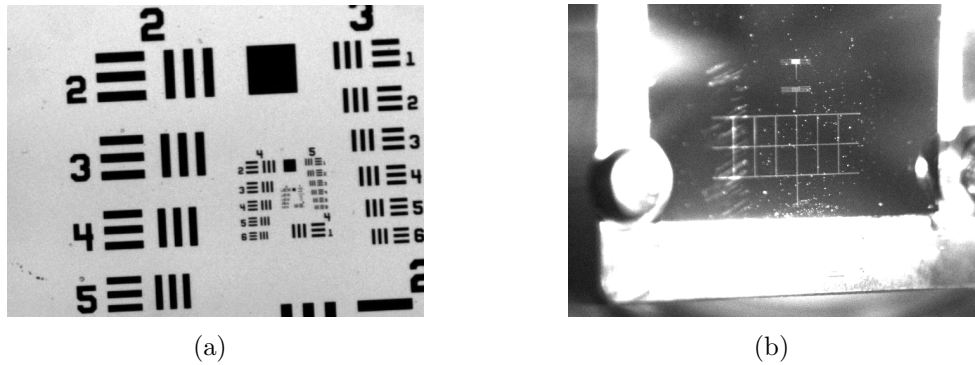
Figure 4.9. The "USAF" Resolution Target (a) and the line grid lithographed on the OTR screen surface (b).

The magnification and the resolution of the images for various lenses setup have been measured using a "Thorlabs" Calibration target based on the well known "USAF 1951" target (see Figure 4.9). In order to estimate the magnification (M) one needs to count the number of pixels (N) of a known size object (L): knowing the pixel size of the camera sensor (R), it will be $M = RN/L$. In a machine, the calibration target is directly lithographed on the top border of each target (i.e. a series of lines made of aluminum on a silicon surface as in Figure 4.9) or is incised on the support frame (if there is no offset between the screen surface and the frame itself). In a laboratory, instead, specifically designed calibration targets are used like the Grid dot, the Variable Line Grating or the "USAF"; the last two types of target allow also resolution evaluations.

The "USAF" target is characterized by different series of black lines with a length equal to $2.5/x$ millimeter for the long side, and $0.5/x$ millimeter for the short side; here the parameter x depends on which series of lines one decides to analyze. This parameter can be calculated with the formula $x = 2^{Group+(Element-1)/6}$, where $Group$ and $Element$ define the series of line chosen [78].

This target has been used to characterize different objectives at different distances in order to find the best solutions for each diagnostic station in terms of magnification, resolution and field of view. Furthermore, the choice of the more appropriate magnification (hence, of the optic system) is also related to the number of photons per pixel collected, as it will be explained in the Section 4.6. The results in terms of magnification are summarized
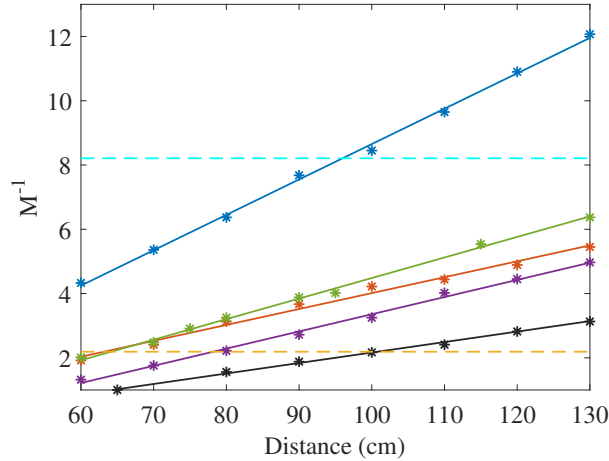
Figure 4.10. Inverse of the magnification as a function of the distance between the target and the camera sensor for different objectives. The blue line (fit) and dot (data) represent the 105 mm; the red ones the 105 mm with teleconverter 2x; the green ones the 180 mm; the black ones the 180 mm with teleconverter 2x and the magenta ones the 180 mm with teleconverter 1.4x. The dashed cyan line represents the magnification required in order to image all the OTR target (3 cm), while the brown one represents the magnification needed for imaging a beam of 1 mm size (see Table 4.6).

in the Figure 4.10; it can be seen that the only lens that allows to reach a magnification equal to 1 with the above mentioned geometric constraints is the 180 mm with a teleconverter 2x. On the other hand, the increase of the focal length (f) limits the minimum magnification achievable in the same distance range; hence, also the field of view is limited. Therefore, a compromise between maximum magnification and a higher flexibility in magnification range achievable needs to be done; this flexibility is useful for instance during the conditioning of the machine, when a change of the beam parameters may require a fast change of the diagnostic setup. Lenses with higher focal length (i.e. 300 mm) can not be used with the current diagnostic stations due to geometric constraints.

The field of view is a parameter strictly related to the magnification; it

depends on the camera sensor size and the pixel size. Therefore, the horizontal field of view is given by $W_{[px]}R/M$ with W the sensor width expressed in pixels; for the vertical one, one must substitute the width with the height. In the case of the camera used, these dimensions are 659 px and 494 px respectively; therefore, since the pixel size is 7.4 µm, the minimum field of view observed thus far is approximately 5 mm × 4 mm. Taking in consideration the expected misalignment in the GBS machine, this field of view is big enough to allow the imaging of an off center beam.

In order to evaluate the resolution, the "USAF" target has been used: the goal is to find the smaller line series which are still "distinguishable". Typically, the line series are considered "distinguishable" if their contrast function is greater or equal to 0.1, and the contrast function is defined as the ratio between the difference and the sum of the intensity values of a black line and the following white space. In an ideal case, the contrast function is equal to 1 while, in the real case with finite resolution, this value is below 1. The measurements showed in Figure 4.11 show that the 180 mm lens with
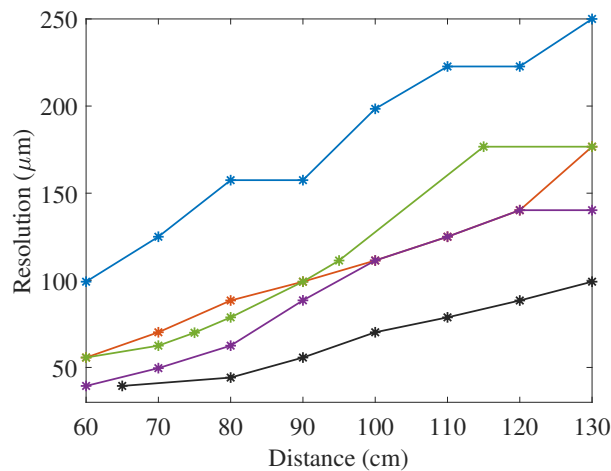
Figure 4.11. Resolution as a function of the distance between the target and the camera sensor for different lens applying the contrast function method. The blue line (fit) and dot (data) represent the 105 mm; the red ones the 105 mm with teleconverter 2x; the green ones the 180 mm; the black ones the 180 mm with teleconverter 2x and the magenta ones the 180 mm with teleconverter 1.4x.

teleconverter 2x is the best choice, with a resolution of 31 µm.

In order to obtain a good flexibility (in terms of magnification), lenses with variable focal length (in the 75 mm - 200 mm range) were also tested: however, the results in terms of resolution did not meet the requirements.

A camera with a different pixel size ($3.75\,\mu m$ instead of $7.4\,\mu m$) has been tested too; however, the overall resolution does not change too much ($\approx 3\%$). This is because the contribution of camera sensor to the overall resolution is small with respect to the other contribution related to the objective, lens aberrations, etc.

Another method to evaluate the resolution is based on the analysis of the Modulation Transfer Function (MTF): the MTF is the Fourier transform of the Line Spread Function (LSF) which is the derivative of the profile of the black rectangle of the "USAF" target [71] (the so called Edge Spread Function). The abscissa at which the MTF is equal to 0.1 represents the maximum line pairs per millimeters achievable; of course, the inverse of it is the resolution. Another way to measure the MTF is to evaluate the contrast function of a so called "Variable Line Grating Test Target" [78]. Finally, optics simulation softwares like ZEMAX allow to calculate the MTF of an optic system and thus the resolution as it can be seen in Figure 4.12. Indeed, Figure 4.12 shows the MTF of a 180 mm objective (blue line) and the 0.1 value that is used to evaluate the resolution: the resulting spatial frequency is about 33 line pairs per millimiters which corresponds to a resolution of about $30\,\mu m$.
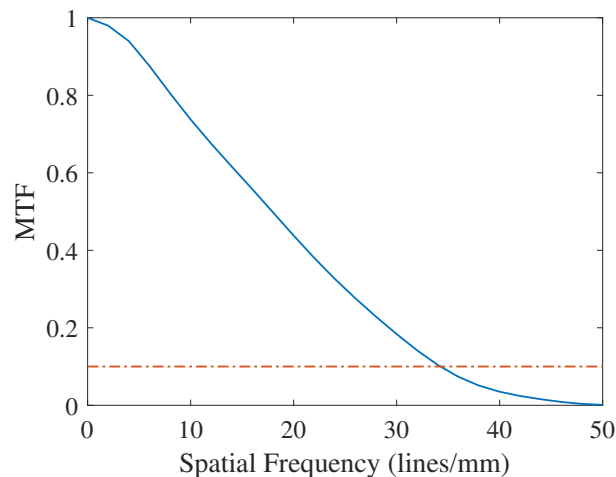
Figure 4.12. MTF evaluation by means of ZEMAX simulations (blue line); the red dot-dashed line represents the value MTF equal to 0.1. Hence, the optic system under test is a 180 mm objective and the resulting resolution is $30\,\mu m$.

The resolution determines how accurate can be a measurement of the beam spot size; a finite resolution implies an uncertainty on the position of each pixel of the acquired beam image. Therefore, one can imagine a "macro-pixel"

with dimension equal to the resolution: hence, the effect of a finite resolution is a down sample of the beam distribution with potentially negative effect on the evaluation of the position and size of the beam. Assuming a Gaussian
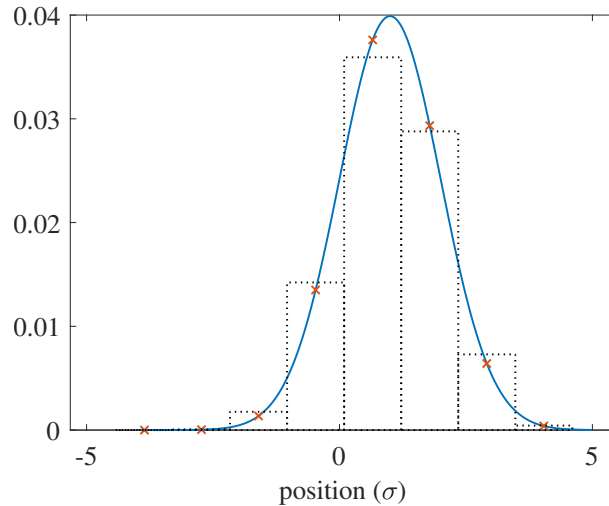
Figure 4.13. Gaussian distribution considered in $\pm 4\sigma$ down sampled with 8 samples (red asterisk).

transverse profile for the beam, one can consider the full beam included in $\pm 4\sigma$. Due to the down sampling, the Gaussian curve is characterized by a number of points (samples) related to the resolution, and their intensities are given by the integral of the black rectangles as seen in Figure 4.13. One can estimate the mean and the standard deviation from these samples and, comparing them with those of the real distribution, one can get an evaluation of the accuracy. In Figure 4.14 these results are summarized: it can be seen that the error in the accuracy decays quite rapidly, and it became negligible with about 20 samples for the evaluation of the σ and 10 samples for the mean. Indeed, the mean value of the Gaussian distribution is less affected.

It is interesting to note that an error below $4\,\%$ is achieved with 8 samples in $\pm 4\sigma$, hence the resolution must be lesser or equal to the σ value. Therefore, with a resolution of $30\,\mu\text{m}$, it is possible to measure with acceptable accuracy beams with σ not smaller than $30\,\mu\text{m}$; or else, in order to measure accurately enough a beam with a $10\,\mu\text{m}$ σ, one needs to achieve at least a resolution of $10\,\mu\text{m}$.
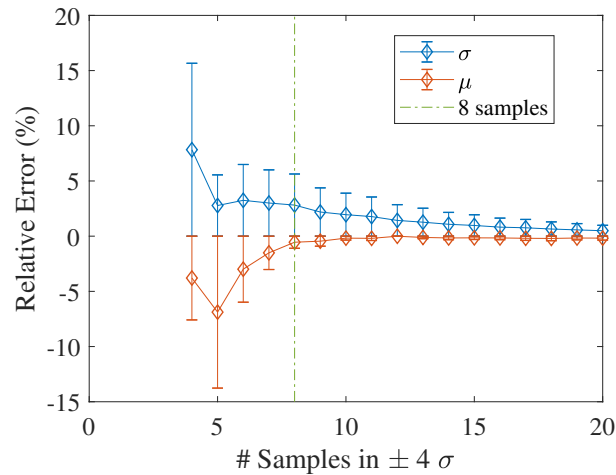
Figure 4.14. Accuracy relative error of the mean μ (red) and the σ (blue) (and relative error bars) of a Gaussian distribution as a function of the number of samples achieved in $\pm 4\sigma$ (averaged over 300 measurements). The green dot-dash line represents the 8 samples case.

4.5.1 Calibration Procedure

In the diagnostic modules installed, a line grid is used for calibration purpose, instead of the USAF target; these line grids (i.e. line spacing of $2\,\text{mm}$) are directly lithographed in the OTR screen itself. A Matlab routine has been designed for the calibration: it takes as an input the acquired image and the line spacing and, counting the pixels separation with the "*findpeaks*" tool, it gives the calibration as an output (see Figure 4.15).

The same Matlab routine can be used with "USAF" images: however, due to the thickness of the lines, the *risetime* and *falltime* tools are more appropriate for the pixel calculation. These tools allow the choice of start and end of the high value as a percent of the maximum value: ideally, one should choose 100% since the "USAF" grid is a square wave signal. However, due to the finite resolution and a not perfectly "in focus" image, the slopes of the rise and the fall are finite and a 100% value underestimates the size of the line; after different tests, a good value has been find in 90% as can be seen in Figure 4.16. The calibration calculated in this way are closed to the expected from the theory: for instance, in the case of Figure 4.16, the magnification calculated is about 1 and the expected value is exactly 1 at that distance ($65\,\text{cm}$) and with the objective used ($180\,\text{mm}$ with $2x$ teleconverter).
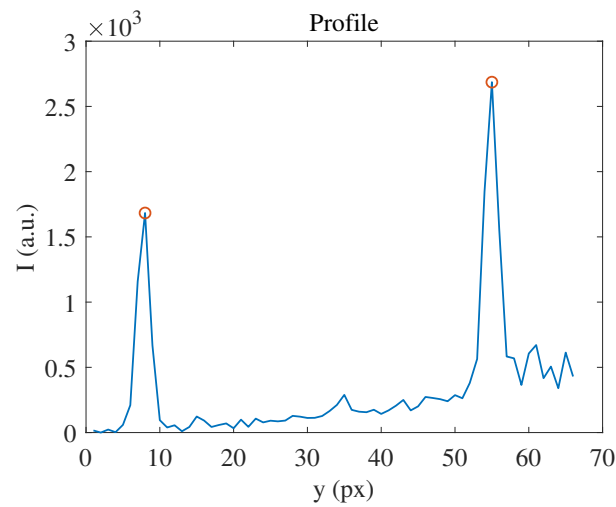
Figure 4.15. Vertical profile of the OTR grid (blue line): the red circles show the centers of the two lines. The line spacing is 2 mm and the measured calibration is $42.55\,\mu\text{m} * \text{px}^{-1}$ (see Figure 4.9).
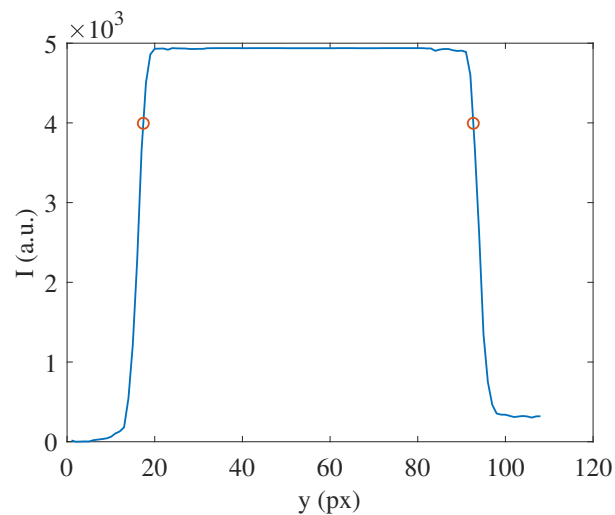
Figure 4.16. Vertical profile of a USAF line (blue line): the red circles show the 90% levels of the *rise* and *fall*. The line length is 557 µm (*Group* and *Element* equal to 2) and the measured calibration is $7.4\,\mu\text{m} * \text{px}^{-1}$ (see Figure 4.9).

4.6 Photon Counting

Another parameter that must be taken into account is the amount of radiation that reaches the camera; it has an effect on the Signal to Noise Ratio (SNR), and therefore the intensity resolution of the optic system. Typically, this quantity is evaluated as the number of photons that are collected by the optical system; conventionally, an accepted value is around 1000 photons per

pixel.

Different parameters affect this value, starting from the way the radiation is generated: a scintillator screen generates more photons than the OTR (see section 4.7.1). The bandwidth of observation (i.e. optical filter to reduce chromatic aberration) and the collecting angle of the optic system have also a large impact on the number of photons, as well as the CCD quantum efficiency which is wavelength dependent. Moreover, the reflectivity of the OTR screen reduces further the number of photons generated: the silicon screens that will be used in the ELI-NP-GBS Linac have a reflectivity halved respect to the aluminized one. Finally, a large magnification spreads the radiation into a large number of pixels, decreasing the number of photons per pixel. Therefore, in this section some consideration has been done to find the right optic system for each diagnostic station.
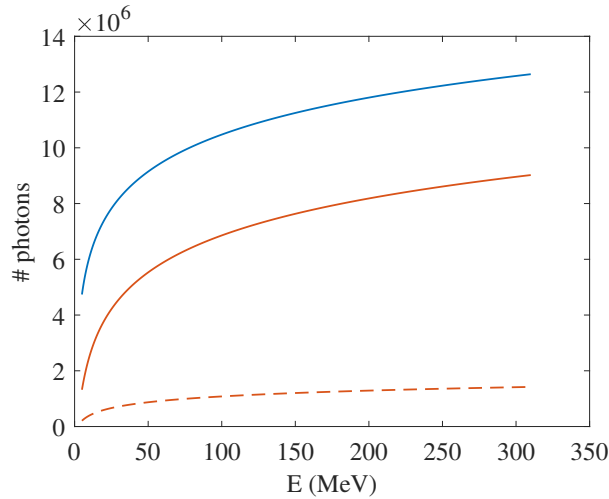
Figure 4.17. Photons generated by means of OTR by a 250 pC beam at different energies (blue line). The red lines represent the collected photons by an optic system in case of $\phi = 0.3$ with (dashed line) or without (continuous line) a green filter.

In order to estimate the amount of radiation that can be generated by the OTR target and collected by the optic system, one can derive from the Equation 3.5 the following [79]:

$$n_g(\lambda_1, \lambda_2) = \frac{Q}{e} \frac{\alpha \ln(4\gamma^2 - 1)}{\pi} \ln\left(\frac{\lambda_2}{\lambda_1}\right) R, \qquad (4.9)$$

where n_g is the number of photons generated by the OTR as a function of the

bandwidth of observation, the beam charge Q and the beam energy γ; α is the fine structure constant and R is the material reflectivity. Figure 4.17 shows the number of photons generated by a 250 pC bunch at different energies; it shows also the number of photons collected assuming a collecting angle ϕ of 0.3 rad and the possibility to use a green filter to reduce chromatic aberrations.
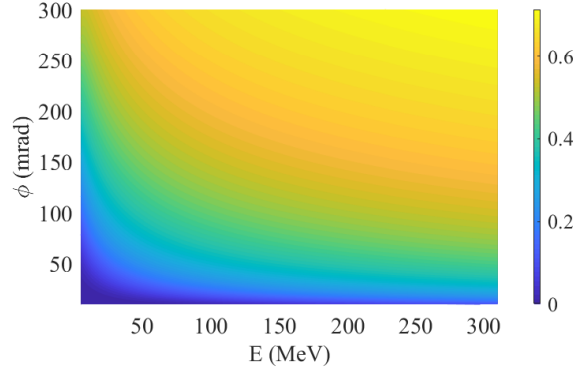
Figure 4.18. Collecting efficiency of an optic system as a function of the beam energy and the collecting angle. Here, the CCD quantum efficiency and the transmissivity of the lens is not taken into account.

The number of photons that are actually collected by the optic system, n_c, are related also to the collecting angle $\phi = \arctan(0.5D/a)$, where D is the lens diameter and a is the distance between the lens and the target; the number of collected photons can be expressed as:

$$n_c(Q, \phi, \lambda_1, \lambda_2) = \frac{\alpha}{\pi} \frac{Q}{e} \ln\left(\frac{\lambda_2}{\lambda_1}\right) \left[\ln\left(1 + 4\gamma^2 \tan^2 \frac{\phi}{2}\right) + \frac{\cos\phi}{1 + \gamma^2 \sin^2 \phi} - 1\right].$$

(4.10)

The ratio between the collected photons and the generated photons gives the collecting efficiency of the optic system (see Figure 4.18): the efficiency increases with the beam energy and with the collecting angle. However, a larger collecting angle means a lens with a larger diameter or closer to the source which may not be possible due to geometrical constraints of the machine; another possibility to increase the angle could be the opening of the diaphragm, but this is not a good idea since it increases chromaticism and other aberrations and it reduces the depth of field.

Finally, the number of photons per pixel is given by Equation 4.11, where
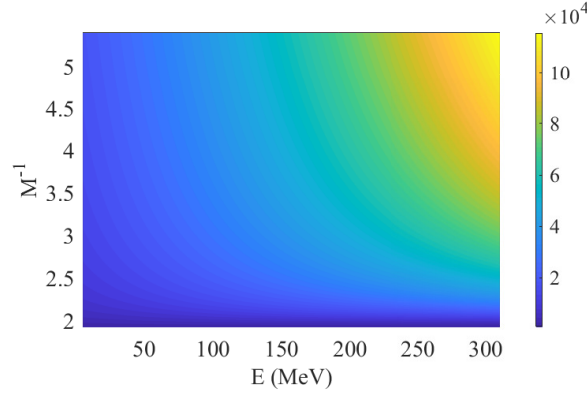
Figure 4.19. Number of photons per pixel as a function of the beam energy and the magnification in the case of a 105 mm Macro lens with a 2x teleconverter (diameter of 78 mm and distance from the source in the range 60 cm × 130 cm).

$\Delta_{x,y}$ are the calibration factor (see Section 4.5) and η_{CCD} is the CCD quantum efficiency (46% for the Basler [32] and 82% for the Hamamatsu [33]).

$$n_{pixel} = n_c \eta_{CCD} \frac{\Delta_x \Delta_y}{2\pi\sigma_x\sigma_y}. \qquad (4.11)$$

It can be seen from Equation 4.11 and Figure 4.19 that also the magnification plays a role in the determination of the number of photons per pixels among with the beam energy and the charge density; therefore, the magnification must be chosen with also this parameter in mind and not only based on field of view consideration. In Table 4.6 the choices made for some ELI-NP-GBS diagnostic stations are summarized.

The same approach needs to be followed for the acquisition of the angular distribution: the number of collected photons is calculated with the same Equation 4.10. As it was shown in Chapter 3, at low energy the angular distribution is spread, hence, the number of photons per pixel is low. On the other hand, at high energy the radiation is more intense and narrower: therefore, the number of photons per pixel is higher. A relay lens system may increase the energy resolution since it magnifies the angular distribution, however it spread also the photons among the pixels reducing the photons density (See Chapter 5).

Another parameter that may affect the accuracy of the measure is related to the detection system: indeed, the sampling of the CCD sensor (finite number

Table 4.6. Optical System proposed for ELI-NP-GBS in order to measure the spot size of the beam (all the lenses are equipped with a teleconverter 2x). The calibration factor is estimated considering the minimum distance achievable in order to have more than 1000 photons per pixel in the camera with a 8 nC pulse train and with a green filter and a Basler camera.

$\sigma_x(\sigma_y)$	γ	**Lens**	**Calibration**	**Resolution**
(µm)		(mm)	$(\mu m * px^{-1})$	(µm)
298 (298)	159	105	15	56
251 (252)	264	105	15	56
211 (213)	264	105	15	56
184 (184)	264	105	15	56
47.5 (109)	560	180	7.4	31
241 (27.4)	560	180	7.4	31
106 (70)	560	180	7.4	31

of pixels) introduce an uncertainty on the position of the peak of intensity. This uncertainty is given by the pixel dimension divided by the square root of 12; applying the propagation of uncertainties, the relative accuracy of the energy measurement can be written as in Equation 4.12:

$$\frac{\delta\gamma}{\gamma} = \frac{\delta\theta_M}{\theta_M}, \tag{4.12}$$

where θ_M is the value at which the intensity is maximum (hence is equal to $1/\gamma$) and $\delta\theta_M$ is its uncertainty. For a fixed detection system, the accuracy decrease with an increase of the energy: for instance, for an energy of 80 MeV and an optical system with focal length of 180 mm and pixel size of 6.5 µm, the relative accuracy error expected is around 0.2%; while for an energy of 234 MeV with the same optical system, the accuracy error is around 0.5% and with a 2 GeV beam the accuracy error is around 2%. Changing the optical system, reducing the pixel size or increasing the focal length as the energy increase, has a beneficial effect on the accuracy. Moreover, also the quantization performed by the detector of the radiation intensity impacts the measurement and especially the evaluation of the minimum of intensity (hence the divergence): indeed, the minimum is not located anymore in a single point, but there is a plateau whose dimension is related to the number of bit of the ADC (Analog to Digital Converter) as can be seen in Figure 4.20. In the case of small angles ($\theta << \theta_M$),

the relative intensity varies as about $(2\gamma\theta)^2$ and the extrema of this plateau due to the detection system can be written as in Equation 4.13:

$$\theta_{min} \approx \pm\frac{\sqrt{\eta}}{2\gamma}, \tag{4.13}$$

where η represents the intensity resolution of the detection system [80]. For instance, assuming a 8 bit detector, a $\theta_{min} = 12.5\%/\gamma$ can be observed while with a 12 bit detector, the minimum value goes to $3\%/\gamma$ and for a 16 bit detector (i.e. Hamamatsu [33]) goes to $0.8\%/\gamma$; this may affect the accuracy of the measure and the uncertainties of a fit. Figure 4.20 shows an example for a beam of 80 MeV and a divergence of 25 µrad: for a 16 bit quantization both the uncertainty and the accuracy error are well below the percent level, while for the 8 bit case the accuracy error of the divergence measurement goes around the 10% and the uncertainty reaches the 100% level while the energy measurements are not significantly affected. Furthermore, for higher energies, both the accuracy and the uncertainty improves as Equation 4.13 suggests. Other parameters (i.e. the noise) can affect the real measurements and change
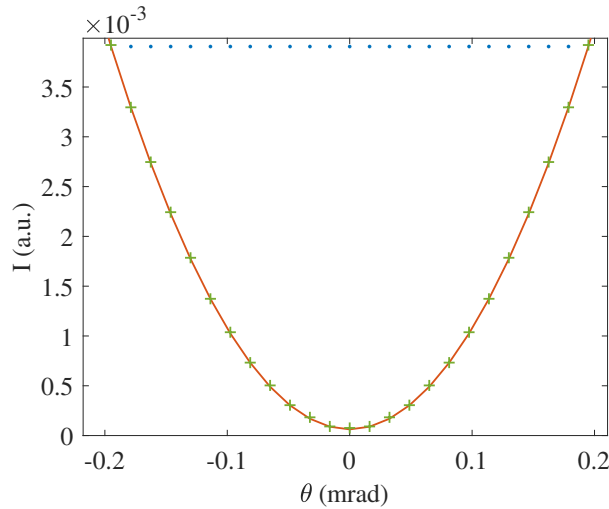
Figure 4.20. Optical transition radiation of a beam with energy of 80 MeV and divergence of 25 µrad (red curve) zoomed around the minimum of its intensity; the green pluses represent the 16 bit quantization while the blue dots represent the 8 bit quantization (only the first level of quantization can be seen with this zoom).

significantly these resolution limits: some of these effects will be treated in Chapter 5.

4.7 Transition Radiation as a Diagnostic Tool

The angular distribution of the transition radiation has been studied as a diagnostic tool for beam energy measurements; however, this radiation is widely used also for beam profile measurements along with other devices like scintillator screens [81] or wire scanner [82].

In a typical monitor setup, the beam is imaged using standard lens optics, and the recorded intensity profile is a measure of the particle beam spot [83]. In conjunction with other accelerator components, it is also possible to perform various measurements on the beam, namely: its energy and energy spread [84, 85] (with a dipole or corrector magnet), bunch length [86] (with a RF deflector), Twiss parameters [87] (by means of quadrupole scan) or in general 6D characterization on bunch phase space [88]. Such techniques are common in conventional [30] and unconventional [89, 90] high brightness Linacs.

Furthermore, it is possible to distinguish the profile monitors between interceptive and non interceptive devices: the scintillator screens and the transition radiation screens are interceptive device, while, for instance, diffraction radiation screens [91] are non interceptive. Diffraction radiation happens when the beam pass through a slit; however, the radiation is weaker than the transition radiation. On the other hand, transition radiation can be considered as a non interceptive technique under some circumstances: indeed, a thin foil of aluminum (or mylar) has been used with highly energetic beam (in the GeV range [92]). The issues are related to the electron scattering of the beam when it passes through the material that increase the overall divergence and hence the beam emittance: when the energy is high enough and the screen is thin (few micron), the scattering contribution can be considered negligible [93].

4.7.1 Comparison between YAG and OTR Screens

In order to perform beam profile and the other above mentioned measurements, also the scintillator screens are widely used; the main advantage is related to the higher radiation intensity. For instance, when a single electron hits a YAG screen, the number of photons that reach the CCD camera is given by the product between the YAG photon yield and the solid angle covered by the optical system [94]; the photon yield grows linearly with the electron

energy (i.e. 35×10^3 ph/MeV [95]) and the number of photons is about five orders of magnitude higher than the transition radiation (see Section 4.6).
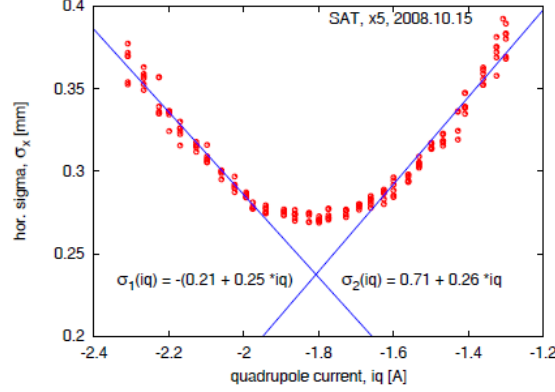
Figure 4.21. Quadrupole scan measurement: approximately between -1.9 A and -1.7 A the saturation happens. The beam charge is 2 nC and the beam waist measured is 280 µm. Picture taken from [94].

YAG screen, however, may pose some issues that may limit their uses: the main issues are the emission saturation, the response time and the resolution achievable. Fluorescence and scintillating screens emits radiation due to the de-excitation of atomic states that was previously excited by the passage of an ionizing particle (i.e. the electron beam): this excitation is proportional to the number of particles only below a certain beam charge density. If a saturation is reached, then the image analysis is not reliable; furthermore, unlike the CCD saturation, the emission saturation is not easy to recognize when observing a single image. Typically, it is observed during a quadrupole scan performed to do emittance measurements: when saturation occurs, in a plot of spot size versus quadrupole current, a plateau is seen instead of a clear waist [94] as can be seen in Figure 4.21. Typical value of charge density that cause saturation is 1.5 nC $*$ mm^{-1}.

Also the response time is related to the physics of the radiation generation of the scintillator screens with the typical values in the order of tens of nanoseconds: for instance, Crytur [95] quotes 70 ns as response time of their crystals. These values are incompatible with the typical bunches separation of most multi-bunch machines like the ELI-NP-GBS where the reference value is 16.1 ns; in these systems a bunch by bunch measurement is not possible with a YAG screen. The transition radiation, instead, is an instantaneous emission

process with a timescale in the order of few femtoseconds [96].

The resolution calculation is more cumbersome to address due to the different parameters that must be taken into account; the observation geometry has a huge impact on the resolution and cause a broad difference in the resolution achievable in the horizontal and the vertical plane, which is less pronounced in the OTR [97]. This discrepancy is explained by the fact that transition radiation is a pure surface effect (the incoming particle field is reflected at the screen surface) while the scintillation light is a volume effect: the radiation source can be approximated by an isotropically emitting line source with an axis determined by the electron beam axis. Among the various scintillator screens, the best resolution is guaranteed by the LYSO:Ce crystal ($Lu_{2-x}Y_xSiO_5$:Ce); also the thickness of the crystal play an important role in the determination of the resolution that increases with the reduction of the thickness. However, from a technical point of view, the handling of thin crystal (i.e. $50\,\mu m$) is rather difficult. Although the typical resolution achieved is on the order of tens of micron, there exist some studies to extend the use of scintillator screens to measure micron size beams [98].

Typically, for high resolution imaging, transition radiation screen and wire scanner are the preferred choices; in case of imaging of small beam with the transition radiation it is common to refer to the so called Point Spread Function (PSF) that defines the minimum beam size that can be resolved using the transition radiation. The PSF was investigated for the first time by Castellano and Verzilov [99] and later in more detail by Potylitsyn [100], Xiang and Huang [101], and Kube [51]. It was shown that the PSF has a double lobe structure which is defined by the wavelength and by the acceptance of the optical system: lowering the wavelength of observation, the resolution is increased as proved by [58]. Another approach is instead based on Point Spread Function dominated beam where the imaged beam can be treated as a convolution between the PSF and the charge spatial distribution: in this situation, the beam size informations can be extracted as shown in these studies [102, 103, 104]. However, the optical schemes proposed suffers from aberrations (mainly spherical and chromatic) that decrease the resolution. In order to solve these issues, some authors propose the use of a Schwarzschild objective that is free of this kind of aberrations [105]: the smaller beam measured is of $1.37\,\mu m$ [106].

Chapter 5

Energy Measurements

In Chapter 3, it was shown the theory behind the OTR and how it is possible to use it for beam energy and beam divergence measurements.

In section 5.2 some consideration on the propagation through the optic system of the OTR produced by an electron beam [107] are shown: this study has been performed with the ZEMAX Optics Studios software [76].

Several studies has been done in order to simulate the OTR radiation in ZEMAX: for instance, at CLIC [108] they study the SPF OTR for different energies (γ up to 4000); Wolfenden [109] studies the radiation propagation at the full optical spectrum. At SPARC_LAB the possibility to simulate the radiation generated by the whole beam has been studied, hence taking into account collective effects [110] (transverse spatial extension and angular distribution).

The simulation results presented here are also validated [111] by experimental data that was taken at the SPARC_LAB test facility [112] (see Section 5.1).

Finally, some of the issues related to the OTR angular distribution dependence on the beam energy are analyzed (see Section 5.3).

ZEMAX is a widely used software in the optics industry as a standard design tool. It is typically used for lens design and illumination devices. The software provides two main analysis modes: the geometrical ray tracing and the physical optics propagation (POP) mode. The former is useful to simulate the behavior of an optical system in the ray approximation, by neglecting any diffraction effects related to the wave nature of the light; however, in order to take into account diffraction effects and polarization, the POP mode is mandatory.

This mode, using diffraction laws, propagates a wave front through an optical system surface by surface; the wave front is modeled at every surface using an array of discretely sampled points, each of them storing complex amplitude information about the photon beam. The entire array is then propagated in free space between optical surfaces. At each optical surface, a transfer function is computed which propagates the beam from one side of the optical surface to the other. To propagate the field from one surface to the other, either Fresnel diffraction propagation or an angular spectrum propagation algorithm is used. ZEMAX automatically chooses the algorithm that yields the highest numerical accuracy. Any source of light can be provided in POP mode: the user has to define the spatial distribution of the complex electric field of the source either in a beam file or in a Windows dynamic link library (DLL).

The DLL functionality was used in order to implement in ZEMAX the SPF OTR. The software offers also some macro functionalities, so called "Zemax Macro Programming Languages" (ZPL Macro): these macros are useful to take into account collective effects on the optical radiation (i.e. chromatic aberration, beam divergence and correlation, and energy spread).

5.1   Energy Measurement Experiment

In Chapter 3 it was shown the equation 3.13 that describes the OTR of particle beam and that we reported here:

$$
\begin{aligned}
I &\propto \frac{\sqrt{\pi}\mu}{\nu}\Re\left[\Phi(z)\left(\frac{1}{2} + \mu\nu z\right)\right] - \mu^2, \\
\mu &= \frac{1}{\sqrt{2}\sigma'}, \quad \Phi(z) = \frac{1 - \mathrm{erf}\,(z)}{\exp\left[-z^2\right]}, \\
z &= \mu(\nu + i\theta), \quad \nu = \frac{1}{\gamma}.
\end{aligned}
\tag{5.1}
$$

Equation 5.1 has been validated experimentally with data taken from the SPARC_LAB high brightness electron Linac [112], that were analyzed in [111]. The feasibility of the fit technique has been verified for beams with different values of charge, energy and divergence as reported in Table 5.1 and with different measurement setup (single shot and time integrated measurements); the two different machine working points are called here "Data set 1" and

Table 5.1. Main beam parameters for two different working points at SPARC_LAB. The values were measured with conventional devices and techniques (beam current monitor for the charge, spectrometer for the energy and quadrupole scan for the beam divergence). The values between brackets represent the uncertainty of the measurements.

	Data set 1	Data set 2
E (MeV)	110.82 (0.07)	123.1 (0.04)
$\Delta E/E$ (%)	0.13 (0.002)	0.06 (0.0002)
Q (pC)	108 (3)	120 (4)
σ'_x (mrad)	0.52 (0.03)	1.1 (0.09)
σ'_y (mrad)	0.66 (0.02)	1.04 (0.09)

"Data set 2". The first working point has lower values of charge, energy and divergence; the optic layout used to observe the angular distribution is the same for the two working points and it has been reported in [55].

Table 5.2. Beam energy and divergence measured at SPARC_LAB for the "Data Set 1" working point and for 3 different configurations (Single shot, 1 second integration and 5 seconds integration). The values between brackets represent the uncertainty of the measurements.

Data set 1	E (MeV)	σ'_x (mrad)	σ'_y (mrad)
Single Shot	105.35 (2.04)	0.72 (0.21)	0.74 (0.17)
10 shots	108.33 (1.53)	0.75 (0.09)	0.77 (0.08)
50 shots	109.87 (0.55)	0.72 (0.04)	0.78 (0.06)

The measurements of the first working point, in the single shot configuration, were affected by a low Signal to Noise Ratio (SNR); the coefficient of determination of the fit (R-square) was 0.65 while the uncertainty was around 1.9 % for the energy and below 30 % for the divergence.

A 1 s integration and a 5 s integration measurements were performed as well: the SNR was increased, as well as the goodness of fit. In the 1 s integration case, for instance, the R-square value became 0.92 while the uncertainty became around 1.4 % for the energy and below 12 % for the divergence. The 5 s integration case, shown in Figure 5.1, gave an R-square value of 0.97 while the uncertainty was around 0.5 % for the energy and below 8 % for the divergence.

Also the accuracy of the measurement, calculated with respect to the values in Table 5.1, is increased: for the energy measurement, it went from

95 % of the single shot case to the 99 % of the 5 s integration case (in the 1 s integration case, the accuracy was 98 %). For the divergence, instead, the accuracy remained around a value of 90 % (see Table 5.2).
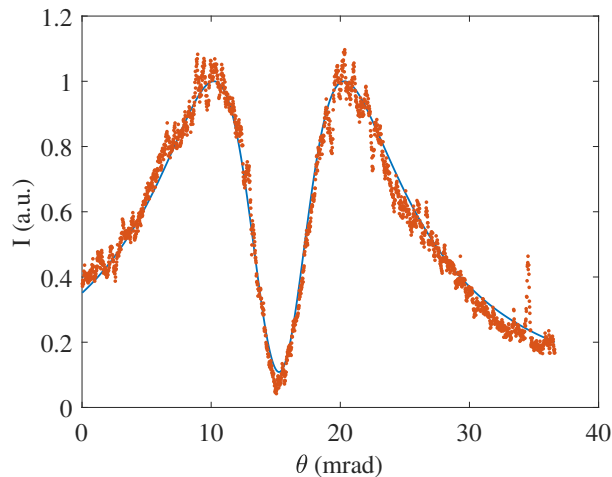
Figure 5.1. Horizontal profile of the OTR angular distribution of a 108 pC beam with energy of 111 MeV and divergence of 0.6 mrad ("Data Set 1" in Table 5.1). The red dots represents the data of a 5 s Integration measurement (the machine operates at a repetition rate of 10 Hz), while the blue line is the fitting curve (Equation 5.1).

Table 5.3. Beam energy and divergence measured at SPARC_LAB for the "Data Set 2" working point and for 2 different configurations (Single shot and 1 second integration). The values between brackets represent the uncertainty of the measurements.

Data set 2	E (MeV)	σ'_x (mrad)	σ'_y (mrad)
Single Shot	122.13 (2.04)	1.4 (0.1)	1.3 (0.1)
10 shots	123.66 (1.02)	1.3 (0.05)	1.2 (0.04)

For the second working point, the measurements were done in the single shot configuration and with 1 s integration; in the first case, shown in figure 5.2, the R-square value was 0.82 while the uncertainty was around 1.7 % for the energy and below 8 % for the divergence.

In the 1 s integration case, shown in figure 5.3, the R-square value was 0.98 while the uncertainty was around 0.8 % for the energy and below 4 % for the divergence.

The accuracy was 99 % for the energy and around 80 % for the divergence in the single shot case, and it increased to 99.5 % for the energy and 85 % for
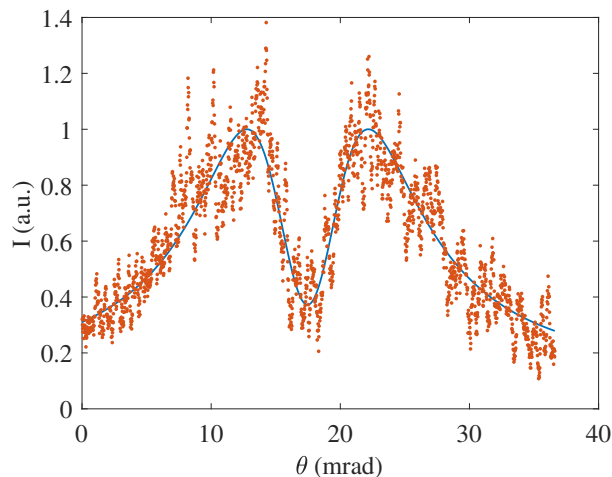
Figure 5.2. Horizontal profile of the OTR angular distribution of a 120 pC beam with energy of 123 MeV and divergence of 1.1 mrad ("Data Set 2" in Table 5.1). The red dots represents the data of a single shot measurement, while the blue line is the fitting curve (Equation 5.1).

the divergence in the 1 s integration case (see Table 5.3).

In order to perform a distributed energy measurement along the GBS, these results were promising: since the OTR intensity is linearly dependent on the charge and, due to the fact that the ELI-NP-GBS bunch charge is 250 pC, this uncertainty and accuracy results are expected for a beam energy around 50 MeV.

Furthermore, the beam energy has an effect on the OTR intensity and on the angular spread; the appropriate optics must be used in order to perform an accurate fit, putting enough points between the peaks and in the tails (a common rule of thumb is to acquire in the range $\theta \in [-3/\gamma : 3/\gamma]$). This can be done changing the focal length (a bigger focal length implies a smaller field of view) or the sensor pixel size; in any case, the same optic system guarantees a wide range of energies (i.e. the one used in this experiment has a focal length of 400 mm and it can measure energies between 30 MeV and 3 GeV but with an increased uncertainty). Moreover, if a single shot measurement is needed, the uncertainty doubles with respect to the 1 second integration case both for the energy and the divergence.

Hence, it can be useful to be able to simulate the radiation through an optic system in order to properly setup a reliable distributed energy measurement.
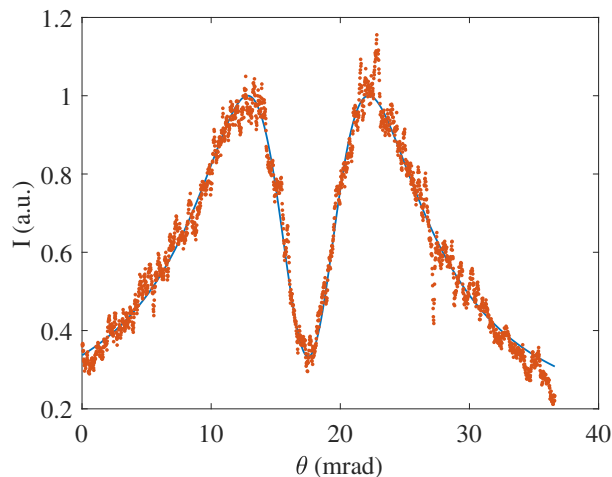
Figure 5.3. Horizontal profile of the OTR angular distribution of a 120 pC beam with energy of 123 MeV and divergence of 1.1 mrad ("Data Set 2" in Table 5.1). The red dots represents the data of a 1 s integration measurement (the machine operates at a repetition rate of 10 Hz), while the blue line is the fitting curve (Equation 5.1).

5.2 Energy Measurement Simulations

In order to implement in ZEMAX the SPF OTR, a DLL with the approximation of the electric field for the OTR induced by a single electron on a target surface [110] has been designed:

$$
\begin{aligned}
E_h &= \frac{e^2}{4\pi^3\epsilon_0 c}\left[\frac{2\pi}{\gamma\lambda}K_1\left(\frac{2\pi}{\gamma\lambda}r\right) - \frac{J_0\left(\frac{2\pi}{\lambda}r\right)}{r}\right]\cos(\phi), \\
E_v &= \frac{e^2}{4\pi^3\epsilon_0 c}\left[\frac{2\pi}{\gamma\lambda}K_1\left(\frac{2\pi}{\gamma\lambda}r\right) - \frac{J_0\left(\frac{2\pi}{\lambda}r\right)}{r}\right]\sin(\phi), \\
r &= \sqrt{(x-x_0)^2 + (y-y_0)^2}, \\
\phi &= \arctan\left(\frac{y-y_0}{x-x_0}\right),
\end{aligned}
\tag{5.2}
$$

with $x - x_0$ and $y - y_0$ the two orthogonal coordinates of the target surface measured from the point of electron incidence (x_0, y_0), γ is the relativistic Lorentz factor, λ is the radiation wavelength, K_1 is the modified Bessel function of first order, and J_0 is the Bessel function of zeroth order. The "h,v" indexes represent the horizontal and vertical polarization respectively; Figure 5.4 shows the vertical polarized SPF OTR and its profile, in *(a)* and in *(b)*, and the

(a)   (b)   (c)
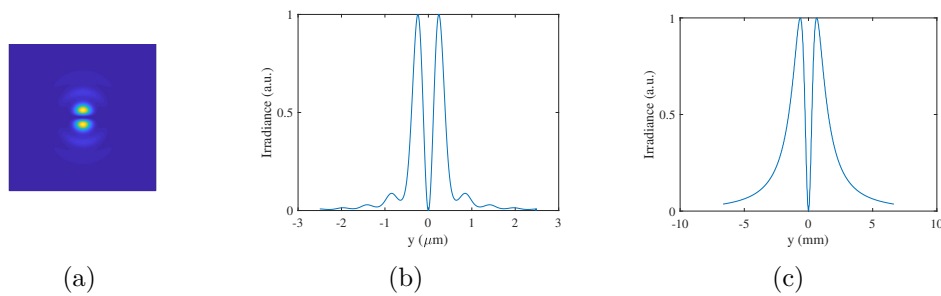
Figure 5.4. Vertically polarized SPF OTR (a) and its vertical profile (b); figure (c) represent the SPF OTR after the propagation through an ideal optical system (paraxial lens with focal length of 100 mm). The detector ("image lens" in ZEMAX) is sampled with a square matrix with dimension of 2048 and a Field of View of 13.312 mm to simulate the "Hamamatsu" camera [33] that is used for the measurements. Also the SPF OTR source was sampled with the same matrix dimension, but with a Field of View of 5 μm. The observation wavelength is 550 nm and the particle energy is 80 MeV.

radiation after the propagation that is in perfect agreement with the theory in *(c)*.

(a)   (b)
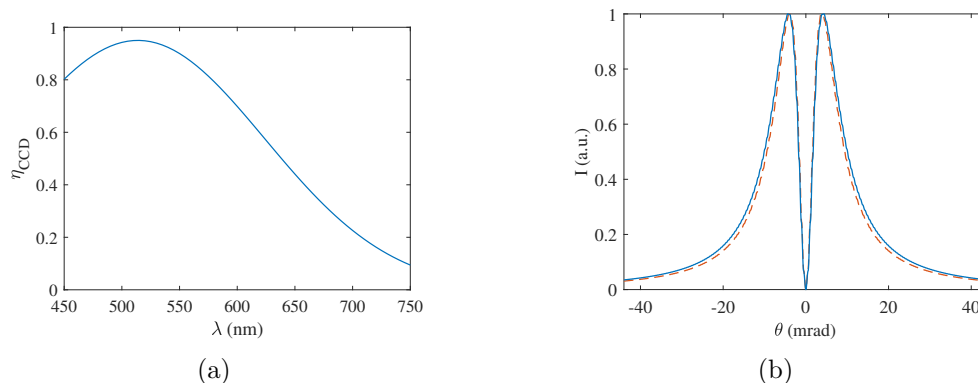
Figure 5.5. CCD Quantum Efficiency (η_{CCD}) as a function of the wavelength λ (a) and horizontal profile of the SPF OTR angular distribution for an energy of 123 MeV. The blue continuous line represents the polychromatic simulation, the red dashed line is the monochromatic one.

The DLL defined in the POP mode propagates only a particle at time and a wavelength at time; in order to take into account the full optical spectrum, one can use the ZPL functionalities provided by the software and implements an appropriate routine. The ZPL macro sets a different wavelength for each simulation and performs a weighted sum of the simulations in order to take into account the variations of quantum efficiency of the used CCD with respect to
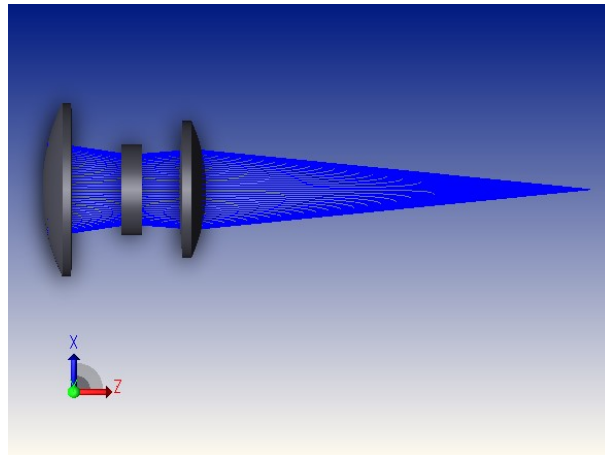
Figure 5.6. Sketch of the optical system used for the simulations: the focal length is 180 mm.

the wavelength (a typical CCD has its maximum efficiency around a wavelength of 550 nm as can be seen in Figure 5.5).

Typically the effects are mitigated by the CCD that acts in a similar way as a 550 nm filter (green): its quantum efficiency frequency dependence is high at the 550 nm wavelength and goes quickly down at the others frequencies. Hence, different CCDs will produce different behavior and they may require the use of an optical filter.

In order to take into account the beam divergence, some authors [109] perform a convolution between the result of the simulation for the single particle and the beam divergence distribution (typically assumed Gaussian). The ZPL macro approach can be used also for evaluating the transverse spatial distribution of the beam and its divergence. The ZPL macro could assume a Gaussian spatial and divergence distribution [110] or it could take the output of a particle tracking code (GPT [113] or Elegant [114]) as the input information about the beam distribution [107] (transverse spatial, divergence and energy distribution): with the latter method, one can evaluate also the effects of the energy spread.

A typical simulated beam is given by tens of thousand of macro-particles: since the ZPL macro propagates one particle at time and sums up the results, the computational time required for the simulation can be very high (an SPF simulation typically requires 30 s). It could be therefore interesting compare the simulation results for different number of macro-particles with the expected theoretical result: this study has been performed for the case of 250, 500
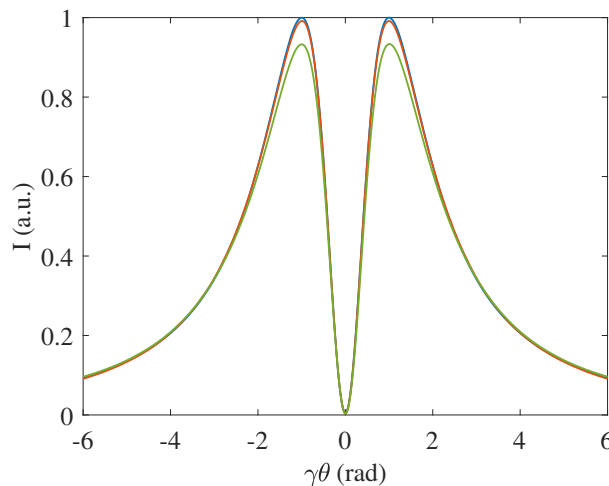
Figure 5.7. Horizontal profile of the beam angular distribution simulated with Zemax at different values of energy spread. The divergence of the beam is $50\,\mu m$ and its γ is 400; the blue line represents a beam with an energy spread of 0.1%; the red line represents a beam with 1% energy spread and the green line is a beam with 10% energy spread. The peak of intensity tends to decrease with the spread while the lobes gets broader. The position of the peaks is still correctly located at $\theta_m = 1/\gamma$.

and 1000 macro-particles and the results do not change significantly with the number of macro-particles: the error committed in the evaluation of beam energy and divergence is well below the percent level as well as the difference between the parameters evaluated for the different simulations. With more than 250 macro-particles, the improvements does not justify the increase of computational time; hence, this value will be used for all the future simulations. Furthermore, the optic system used in these simulations is the one showed in Figure 5.6.

In Figure 5.7, it is shown the result of a simulation considering different values of energy spread (0.1, 1 and 10%): the main effects of the energy spread on the angular distribution are a slightly decrease of the peak intensity of radiation and a broadening of the two lobes. The effect is very weak at these values of energy spread, but it may pose an issue in the reliability of the fit function described in Section 5.1 since it assumes a negligible energy spread. Indeed, the uncertainty of the fit parameters increases of about 10% for the 10% energy spread case and of about 1% for the 1% energy spread case.

Since the ELI-NP-GBS machine is equipped with OTR screen in each diagnostic stations, it is possible to perform a distributed energy measure-

Table 5.4. Beam parameters estimated by "Elegant" code simulation [114]. Here the correlation represents the correlation coefficient.

Position	γ	$\Delta\gamma/\gamma$ (%)	σ'_x (σ'_y) (µrad)	Correlation xx' (yy')	Spot Size $x(y)$
Screen 1	159	1.6	25 (26)	0.972 (0.971)	404 (408)
Screen 2	230	0.6	59 (57)	0.996 (0.995)	323 (318)
Screen 3	459	0.1	47 (45)	0.023 (0.175)	29.4 (19.6)
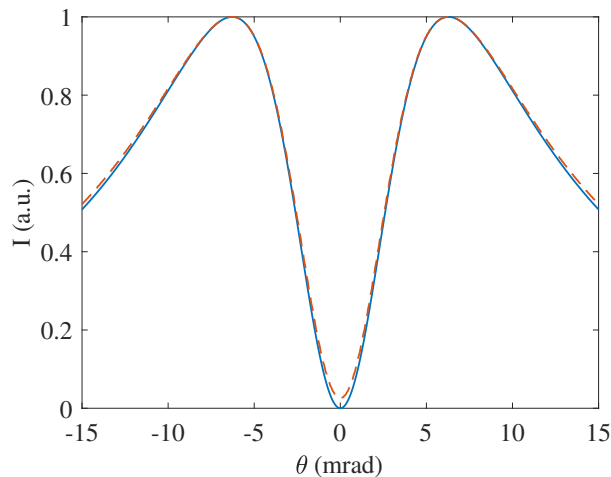
Figure 5.8. Horizontal profile of the beam angular distribution expected for a 81 MeV beam with a horizontal spot size of 404 µm, a 26 µrad beam divergence and a $<xx'>$ correlation coefficient of 0.97 (first line of Table 5.4): the blue continuous line represents the uncorrelated curve (Eq. 5.1), while the red dashed line is the ZEMAX simulation. The beam correlation and the beam size produce an overall divergence higher than the angular spread taken into account in Eq. 5.1

ment along the Linac: this is useful during the commissioning phase of the machine, especially to verify the correct operations of the newly design C Band structure [115]. Figure 5.8 shows how beam size and correlation impact the OTR angular distribution: the energy and divergence have been measured performing a fit of the simulated data and the results are summarized in Table 5.5. The uncertainty for the energy is on the order of few keV and in the µrad scale for the divergence, while the R-Square of the fit is equal to 1. The results in Table 5.5 shows a perfect agreement between simulations and the real beam in terms of beam energy measurements; however, the beam divergence measure is strongly affect by the correlations between the x and the x' plane and between the y and the y' plane. Indeed, as Table 5.4 shows, the beam spot size decreases from one screen to the other as well as the correlation coefficient

Table 5.5. Beam energy and divergence estimated by means of fit technique using Equation 5.1 on the Zemax simulations in the case of correlated beams. The values between the parenthesis refer to the error with respect to the "Elegant" simulation results.

Position	γ	σ'_x(µrad)	σ'_y (µrad)
Screen 1	159 (0.08%)	163 (560%)	158 (516%)
Screen 2	230 (0.04%)	166 (183%)	172 (200%)
Screen 3	459 (0.08%)	51 (8%)	49 (8%)
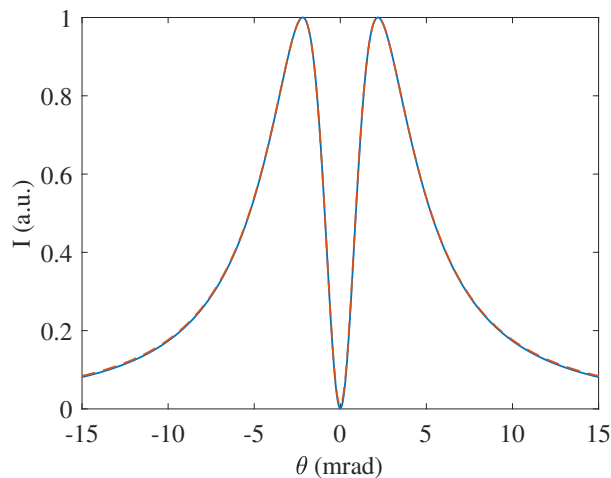
Figure 5.9. Horizontal profile of the beam angular distribution expected for a 234 MeV beam with a horizontal spot size of 30 µm, a 47 µrad beam divergence and a $< xx' >$ correlation coefficient of 0.02: the blue continuous line represents the theoretical curve (Eq. 5.1), while the red dashed line is the ZEMAX simulation. Here, the effects of the correlation and of the beam size are negligible.

(it is close to 1 in the first 2 screens), hence the correlation gives a contribution to the overall measured divergence; furthermore, the uncertainty is affected too. This is due to the fact that Equation 5.1 assume there is no correlation, hence a different equation will better fit the data. A second simulation has been performed not considering the correlations: the transverse position of the particle (x_0, y_0 in the Equation 5.2) is not pass through the ZPL routine. In this second case, there is indeed a better agreement with the theory: table 5.6 summarizes these results.

In any case this simulation method proved to be very robust in the energy measurement evaluation. Furthermore, these routines may be useful in combination with some specific optic system (i.e. an array lens) in order to measure also the beam correlation: for instance, this is particularly of interest when

Table 5.6. Beam energy and divergence estimated by means of fit technique using Equation 5.1 on the Zemax simulations in the case of uncorrelated beams. The values between the parenthesis refer to the error with respect to the "Elegant" simulation results.

Position	γ	σ'_x(µrad)	σ'_y (µrad)
Screen 1	159 (0.02%)	26 (4%)	26 (0.3%)
Screen 2	230 (0.004%)	57 (2%)	54 (5%)
Screen 3	459 (0.03%)	51 (8%)	49 (8%)
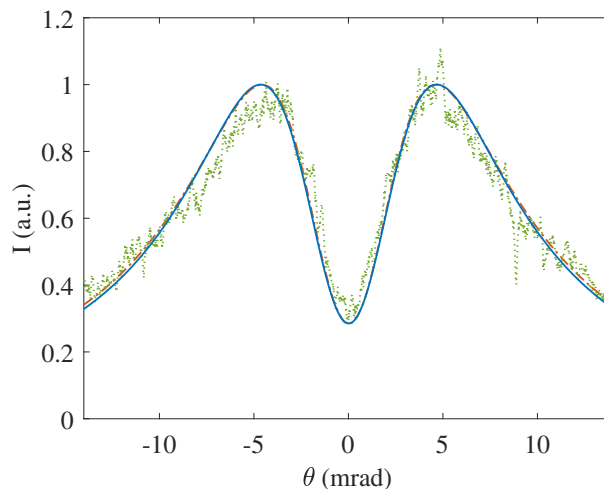
Figure 5.10. Horizontal profile of the beam angular distribution for an energy of 123 MeV and a divergence of 1.1 mrad ("Data set 2"): the blue continuous line represents the theory (Equation 5.1), the red dashed line is the ZEMAX simulation and the green dots represent the experimental data.

designing the optic setup for single shot emittance measurements [55].

This method has been also experimentally validated using the data taken from SPARC_LAB already analyzed in Section 5.1, specifically the so called "Data set 2".

5.3 Energy Measurement Design

If one wants to perform a distributed energy measurement, he needs to take into consideration the required field of view and resolution at different beam energies: at low energies, since the angular distribution is wide, one has to put the optics close to the source in order to view the radiation in the camera. At high energy, instead, the angular distribution is narrow: in order to resolve
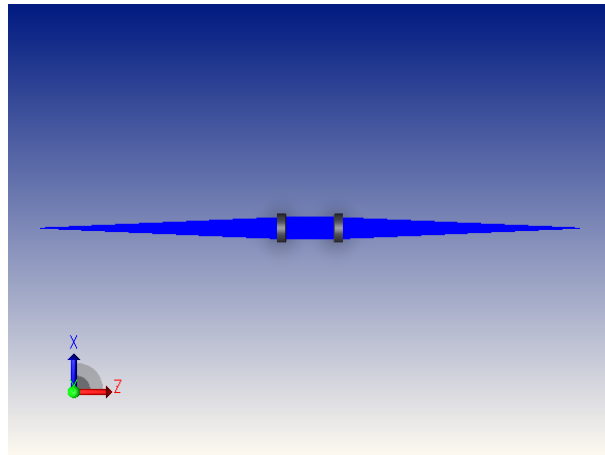
Figure 5.11. Sketch of the proposed layout based on relay optics. The appropriate choice of the focal lengths f_1 and f_2 allows to obtain any angular magnification and, therefore, the same horizontal resolution on the CCD camera.

the minimum and the two maxima of the distribution, one needs to let the radiation propagates for a long drift before collect it with the optic system. However, having the camera too close to a source of radiation may damage the camera itself; on the other hand, a long free space propagation may not be feasible due to geometric constraints.

A solution could be a relay optics system (see Figure 5.11): with this system, with an appropriate choice of the focal length and the relative distances, the source is replicated and eventually magnified at a distance that fits the machine constraints. Typically, one wants to acquire the distribution in the range $\theta \in [-3/\gamma : 3/\gamma]$ in order to have enough points between the two maxima and to cut the parts of the tails that are affected by the noise: for instance, for a CCD with $2048x2048$ pixels of $6.5\,\mu\text{m}$ size like the "Hamamatsu Orca-Flash4" [33], this means to have about 460 pixels between the two maxima. If one call L, the distance between the last lens and the CCD and x_M the position of the maximum of the distribution, one can easily find that $x_M = f_1(L - f_2)/(f_2\gamma)$: for instance, for an energy of $5\,\text{MeV}$, one solution could be f_1 equal to $20\,\text{mm}$, f_2 equal to $10\,\text{mm}$ and L equal to $17\,\text{mm}$ in order to have 430 pixels between the two maxima of the angular distribution. For an energy of $320\,\text{MeV}$, one could choose f_1 equal to $200\,\text{mm}$, f_2 equal to $20\,\text{mm}$ and L equal to $120\,\text{mm}$ in order to have 490 pixels between the two maxima of the angular distribution.

Chapter 6

Bunch by Bunch Measurement

In a high charge multibunch system, issues related to beam loading and wakefields [116] may arise. It is therefore fundamental evaluate the effects that this phenomena may cause on the different bunches along the pulse train: this will be done measuring a single bunch of the pulse train with a gating camera system. The gating window will be chosen below the bunch separation (i.e. 16.1 ns in the ELI-NP-GBS case) and it will be triggered on a specific bunch of the pulse train (i.e. first bunch of the pulse train, then the second bunch of the next pulse train, and so on).

Due to the weak intensity of the OTR, a gain intensifier is needed: this requires a characterization of the intensifier as well, in order to take into account its non linearities and to avoid saturation or low Signal to Noise Ratio (SNR) that may false the measurements [117].

In section 6.2 measurements taken with the synchrotron radiation at the Dafne facility [118, 119] are shown.

6.1 Camera System

The camera system is composed by three main elements: an intensifier, a tube lens and a camera as can be seen in Figure 6.1; the tube lens is used to recreate the image acquired by the intensifier in the camera sensor, eventually with a magnification. In the case of the experiments that will be described in Section 6.2, the magnification is equal to 1 and so, the image on the camera is an exact replica of the image in the intensifier. The camera is the Hamamatsu Orca-flash4 [33] which uses a high sensitivity CMOS sensor: the quantum efficiency

Figure 6.1. Picture of the gated camera system: on the left side it is placed the intensifier, while on the right side there is the CMOS camera. The devices are linked by a tube that realizes a magnification equal to 1.

peak is 82% at a wavelength of 550 nm and its spectral response is showed in Figure 6.2. The number of pixels are 2048 both horizontally and vertically and the pixel size is 6.5 µm: hence, the effective area is 13.312 mm × 13.312 mm.
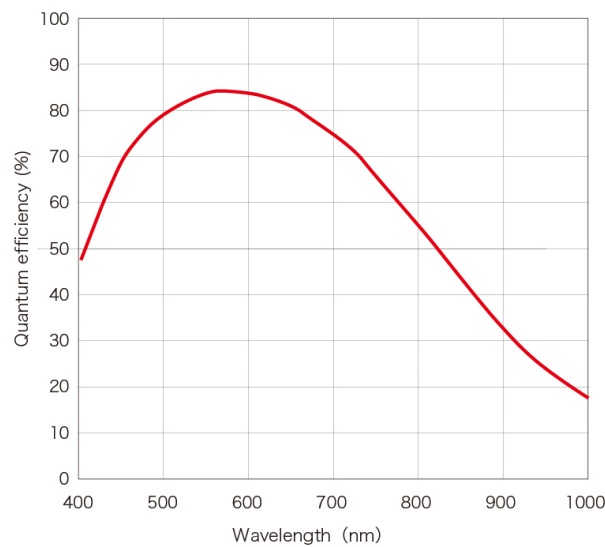
Figure 6.2. Plot of the sensor quantum efficiency as a function of the wavelength. Picture taken from [33].

The intensifier acts also as a gating device with two different operating mode: the main mode applies the gating to the photocathode (GaAsP) with a dedicated circuit. A second circuit allows to gate also the Multi-Channel Plate (MCP): this is useful when acquiring Ultra Violet light image, or the gate time is long, since it improves the extinction ratio and it reduces the background noise. The drawbacks are that the delay time of the pulse is increased of
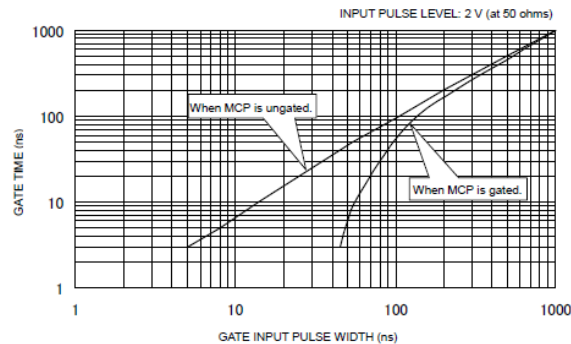
Figure 6.3. Plot of the gate time window as a function of the input pulse width coming from the Stanford signal generator. Typically, the MCP is gated when an improvement of the extinction ratio is needed (i.e. when observing UV light image). Picture taken from [33].

50 ns and the maximum repetition rate allowed is reduced to 10 kHz instead of 30 kHz. Furthermore, as showed in Figure 6.3, the actual gate time may be different from the input pulse width. Since the bunch separation in the ELI-NP-GBS case is 16.1 ns, only the principal gate circuit is used.

The intensifier allow to set the gain of intensity in the range $600 - 990$ that means an actual gain between 16 dB and 43 dB with an envelope that is almost linear in a logarithmic scale as can be seen in Figure 6.4

6.2 Measurements

In order to evaluate the effects of the Gain settings on the transverse spot size measurements, a series of data have been collected at the Dafne facility [118] using the synchrotron radiation. In a ring, the number of photons generated by the beam on each turn is given by the Equation 6.1:

$$N(\lambda) = \sqrt{3}\frac{e}{hc}\gamma I G_1 \frac{\Delta\lambda}{\lambda}\Delta\theta, \qquad (6.1)$$

where e is the electron charge, c is the speed of light, h is the Planck's constant, γ is the beam Lorentz factor, I is the beam current, λ is the observation wavelength, $\Delta\theta$ is the acceptance angle and G_1 is called "Universal Function". The value of the Universal function considering the Dafne critical energy [120] is 0.3; the beam in Dafne consist of a pulse train of 108 bunches with a bunch separation of 2.7 ns, the bunch length is 100 ps and the pulse train current is
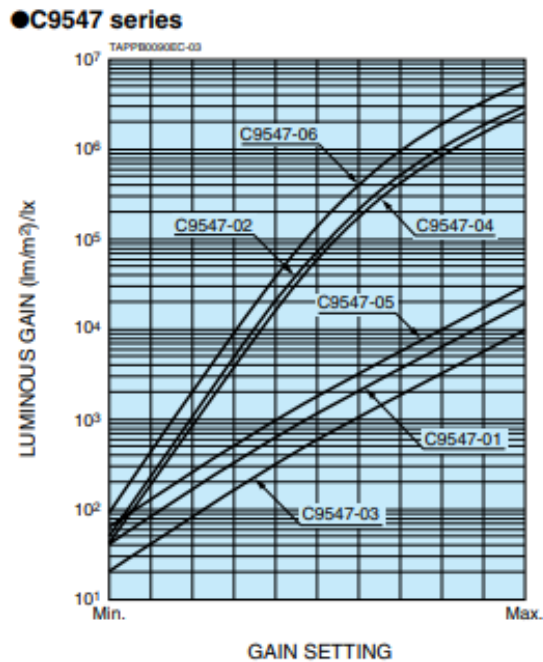
Figure 6.4. Plot of the luminous gain. The intesifier model is the "C9547-01" for which the minimum gain setting is 600 and the maximum one is 990. Picture taken from [33].

650 mA. The beam energy is 500 MeV, the acceptance angle is 1 mrad and the light is observed in the optical spectrum; putting this number in Equation 6.1, one can obtain a value of about 1.3×10^{22} photons per turn. This value is, as expected, higher than the one obtain with a weaker source like transition radiation: indeed, as seen in Chapter 4, the number of photons expected in the ELI-NP-GBS case is around 1.2×10^7. Furthermore, the revolution frequency of Dafne is 3 MHz while the minimum exposure time of the camera is 3 ms: this means that the image acquired is an integrated measure on at least 9000 turns, or even more depending on the exposure time setting.

The goal of the experiment is to evaluate the spot size measurement as a function of the Gain setting [117]: this was done spanning the Gain setting interval with a step of 50 at different combination of exposure time and gate time.

For instance, Figure 6.5 shows the case of a Gate input pulse of 10 ns, that corresponds to 6 ns effective gate window, and different values of exposure time: with this value of gate window, the detecting system is able to acquire 20 bunches out of 108, hence the number of photons is reduce to 2.4×10^{20}
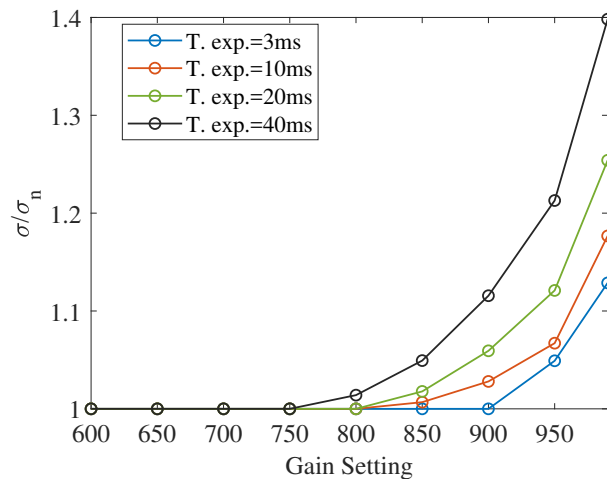
Figure 6.5. Plot of the measured spot size normalized to the expected one as a function of the Gain setting for different values of exposure time: namely 3 ms, 10 ms, 20 ms and 40 ms in blue, red, green and black line, respectively.

photons per turn. Figure 6.5 shows that with a Gain setting higher than 850, saturation arises and this impacts the beam spot measurement; also the plot of the intensity as a function of the gain shows a saturation (see Figure 6.6). It can be also noted that the exponential part of the intensity (below a gain of 850) is in good agreement with the gain specification of Figure 6.4: indeed, an interpolation of those data shows this as can be seen in Figure 6.6.

Another interesting thing to note is the behaviour for a value of the gate length below the minimum declared in the specification (5 ns). If the input length is set to a value below 5 ns, or even if the gate is turn off, the behaviour is not a complete block of the light as expected: some light reaches the CCD and eventually it can be intensify. Fixing the values of exposure time (3 ms) and Gain setting (600) and changing the gate length from 5 ns to any value below, or even unplugging the cable or turning off the gate, the intensity is reduce by a factor of about 7 but it does not go to the background noise level. However, two things must be noted: first, the source of intensity is rather high since it comes from a large number of turns in the ring. In a Linac, the intensity expected is indeed much lower. Second, the CCD used is very sensitive to light: the use of a less sensitive camera like a "Basler" [32] with the same beam configuration, does not show this behavior [120].
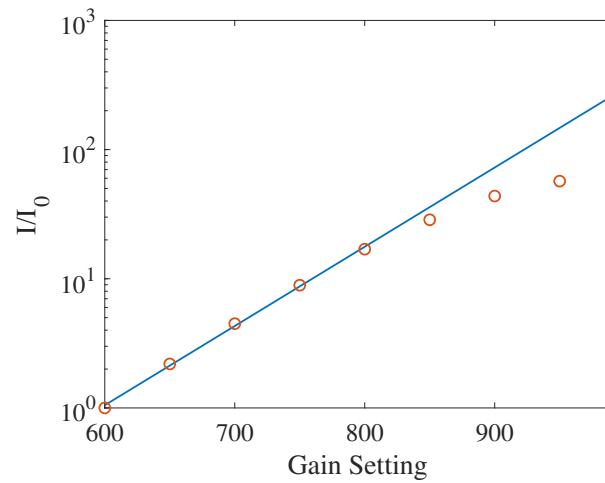
Figure 6.6. Semi-logarithmic plot of the measured intensity normalized to the minimum one (Gain setting of 600) as a function of the Gain setting (red circles); the blue line represents a linear fit of the first 5 data. The Gain in intensity going from 600 to 850 is about 16 dB: by mean of interpolation, the gain at 990 become as expected 27 dB.

Chapter 7

Conclusions

This Ph.D. work has been performed in the framework of activities of the Diagnostic group of the Frascati laboratories of INFN, related to the ELI Nuclear Physics Gamma Beam System (ELI-NP-GBS) project.

In the ELI-NP-GBS, a high power Laser pulse is Compton scattered with an electron beam generated through an high brightness Linac. In this way a highly polarized, and nearly mono-energetic γ-Ray beam with a tunable energy from about $0.2\,\mathrm{MeV}$ to $19.5\,\mathrm{MeV}$ and a high spectral density ($104\,\mathrm{photons} * \mathrm{eV} * \mathrm{s}^{-1}$) is produced. This unique γ-Ray beam has a wide range of applications from nuclear physics to astrophysics, from medical research to homeland security and industrial applications.

The high photon beam performances impose strong requirements on the electron beam, thus on the diagnostic measurements setup. The Linac is required to achieve a normalized emittance in both directions lower than $0.5\,\mathrm{mm} * \mathrm{mrad}$ and an energy spread below 0.1%. Moreover to increase the maximum photon flux the Linac has to work in multibunch mode (32 bunches per pulse) with a repetition rate of $100\,\mathrm{Hz}$. Since the performances of the RF system obviously affect those of the electron beam, great care is needed in its commissioning: hence, the availability of diagnostics measurements after each RF module (i.e. BPMs, Beam screens) may be very useful. In particular, in this dissertation, the possibility to perform a distributed energy measurement along the Linac has been presented.

Overall, in the Linac 23 beam diagnostic stations are mounted, each equipped with both YAG and OTR screen; this screens are mainly used for beam spot size measurements. In conjunction with other accelerator com-

ponents, it will also be possible to perform various measurements on the beam, namely: its energy and energy spread (with a dipole or corrector magnet), bunch length (with an RF Deflector), Twiss parameters (by means of quadrupole scan) or in general 6D characterization on bunch phase space.

The high beam charge density and the multibunch mode in the ELI-NP-GBS may pose issue related to the thermo-mechanical stress due the energy that the beam deposits in the screen; a theoretical and a numerical study has been performed pointing out the need to use a pure silicon screen instead of the widely used aluminized screens. The silicon screen still allows a good quality diagnostic with a better resistance to thermo-mechanical stress.

The optical diagnostic stations has been characterized in terms of magnification and resolution achievable; a set of configurations that fits well the resolution specification for the different beam parameters along the Linac has been chosen. Namely, a "Basler Scout A640-70gm" CCD camera with a lens and a teleconverter. Furthermore, in order to perform bunch by bunch measurements, a gating camera system has been tested and characterized.

Moreover, the OTR screens allow to retrieve the beam energy by mean of angular distribution measurements; this, combined with the capillary presence of the screens along the machine, allows to perform a distributed energy measurements of the beam along the Linac.

The Transition Radiation has been characterized from the theoretical point of view and with the optic simulation software Zemax, and validated with experimental data taken from SPARC_LAB. The Zemax implementation allows to study the transport of the radiation trough an optic system and to take into account collective effect such as beam divergence, correlation and energy spread or to study the impact of chromatism in the measurement.

Bibliography

[1] M. Marongiu *et al.*, "Thermal behavior of the optical transition radiation screens for the eli-np compton gamma source," *Nuclear Instruments and Methods in Physics Research Section A: Accelerators, Spectrometers, Detectors and Associated Equipment*, 2016.

[2] F. Cioeta *et al.*, "Thermal issues for the optical transition radiation screen for the eli-np compton gamma source," in *8th Int. Particle Accelerator Conf.(IPAC'17), Copenhagen, Denmark, 14-19 May*, 2017, pp. 246–249.

[3] M. Marongiu *et al.*, "Optical issues for the diagnostic stations for the eli-np compton gamma source," in *8th Int. Particle Accelerator Conf.(IPAC'17), Copenhagen, Denmark, 14-19 May*, 2017, pp. 238–241.

[4] R. H. Milburn, "Electron scattering by an intense polarized photon field," *Physical Review Letters*, vol. 10, no. 3, p. 75, 1963.

[5] F. Arutyunian *et al.*, "The compton effect on relativistic electrons and the possibility of obtaining high energy beams," *Phys. Letters*, vol. 4, 1963.

[6] L. Federici *et al.*, "Backward compton scattering of laser light against high-energy electrons: the ladon photon beam at frascati," *Il Nuovo Cimento B (1971-1996)*, vol. 59, no. 2, pp. 247–256, 1980.

[7] F. Amman *et al.*, "Two-beam operation of the 1.5 gev electron-positron storage ring adone," *Lettere Al Nuovo Cimento (1969-1970)*, vol. 1, no. 15, pp. 729–737, 1969.

[8] C. Vaccarezza *et al.*, "The sparc_lab thomson source," *Nuclear Instruments and Methods in Physics Research Section A: Accelerators, Spec-*

trometers, Detectors and Associated Equipment, vol. 829, pp. 237–242, 2016.

[9] C. Tang *et al.*, "Tsinghua thomson scattering x-ray source," *Nuclear Instruments and Methods in Physics Research Section A: Accelerators, Spectrometers, Detectors and Associated Equipment*, vol. 608, no. 1, pp. S70–S74, 2009.

[10] W. Brown *et al.*, "Experimental characterization of an ultrafast thomson scattering x-ray source with three-dimensional time and frequency-domain analysis," *Physical Review Special Topics-Accelerators and Beams*, vol. 7, no. 6, p. 060702, 2004.

[11] F. E. Carroll *et al.*, "Pulsed tunable monochromatic x-ray beams from a compact source: new opportunities," *American journal of roentgenology*, vol. 181, no. 5, pp. 1197–1202, 2003.

[12] S. Kashiwagi *et al.*, "Compact soft x-ray source using thomson scattering," *Journal of applied physics*, vol. 98, no. 12, p. 123302, 2005.

[13] E. Miura *et al.*, "X-ray generation via laser compton scattering using quasi-monoenergetic electron beam driven by laser-plasma acceleration," in *AIP Conference Proceedings*, vol. 1507, no. 1. AIP, 2012, pp. 304–309.

[14] C. Sun *et al.*, "Theoretical and simulation studies of characteristics of a compton light source," *Physical review special topics-accelerators and beams*, vol. 14, no. 4, p. 044701, 2011.

[15] E. Eggl *et al.*, "The munich compact light source: initial performance measures," *Journal of synchrotron radiation*, vol. 23, no. 5, pp. 1137–1142, 2016.

[16] A. Bacci *et al.*, "The Star Project," in *Proc. of International Particle Accelerator Conference (IPAC'14), Dresden, Germany, June 15-20, 2014*, pp. 2238–2241.

[17] A. Variola *et al.*, "Thomx conceptual design report," *LAL RT*, vol. 9, p. 28, 2010.

[18] E. Eggl *et al.*, "X-ray phase-contrast tomography with a compact laser-driven synchrotron source," *Proceedings of the National Academy of Sciences*, p. 201500938, 2015.

[19] R. Hajima *et al.*, "Proposal of nondestructive radionuclide assay using a high-flux gamma-ray source and nuclear resonance fluorescence," *Journal of Nuclear Science and Technology*, vol. 45, no. 5, pp. 441–451, 2008.

[20] T. Shizuma *et al.*, "Nondestructive identification of isotopes using nuclear resonance fluorescence," *Review of Scientific Instruments*, vol. 83, no. 1, p. 015103, 2012.

[21] V. Petrillo *et al.*, "Photon flux and spectrum of gamma-rays compton sources," *Nuclear Instruments and Methods in Physics Research Section A*, vol. 693, pp. 109–116, 2012.

[22] "The White Book of ELI Nuclear Physics," http://www.eli-np.ro/documents/ELI-NP-WhiteBook.pdf.

[23] C. Vaccarezza *et al.*, "A european proposal for the compton gamma-ray source of eli-np," in *International Particle Accelerator Conference-IPAC'12*. Joint Accelerator Conferences Website, 2012, pp. 1086–1088.

[24] L. Serafini *et al.*, "Technical Design Report EuroGammaS proposal for the ELI-NP Gamma beam System," EuroGammaS, Tech. Rep., 2014.

[25] "EuroGammaS Association," http://www.e-gammas.com/.

[26] L. Serafini *et al.*, "High intensity x/γ photon beams for nuclear physics and photonics," in *EPJ Web of Conferences*, vol. 117. Nuclear Structure, 2016, p. 05002.

[27] K. Dupraz *et al.*, "Design and optimization of a highly efficient optical multipass system for gamma-ray beam production from electron laser beam compton scattering," *Physical Review Special Topics-Accelerators and Beams*, vol. 568, no. 2, p. 033501, 2014.

[28] A. Bacci *et al.*, "Electron linac design to drive bright Compton backscattering gamma-ray sources," *Journal of Applied Physics*, vol. 113, no. 19, p. 194508, 2013.

[29] V. Fusco *et al.*, "Beam dynamics study of a C-band linac driven FEL with S-band photo-injector," in *Proc. of Particle Accelerator Conference (PAC'09), Vancouver, Canada, May, 2009.*

[30] D. Alesini *et al.*, "Status of the sparc project," *Nuclear Instruments and Methods in Physics Research Section A*, vol. 528, no. 1, pp. 586–590, 2004.

[31] M. Ferrario *et al.*, "Experimental demonstration of emittance compensation with velocity bunching," *Physical Review Letter*, vol. 104, p. 054801, 2010.

[32] "Basler Scout scA640-70gm," https://www.baslerweb.com/en/products/cameras/area-scan-cameras/scout/sca640-70gm/#tab=specs.

[33] "Hamamatsu Orca-Flash 4," https://www.hamamatsu.com/sp/sys/en/manual/C11440-22CU_IM_En.pdf.

[34] D. Alesini *et al.*, "RF deflector design and measurements for the longitudinal and transverse phase space characterization at SPARC," *Nuclear Instruments and Methods in Physics Research Section A: Accelerators, Spectrometers, Detectors and Associated Equipment*, vol. 829, pp. 488–502, 2006.

[35] John David Jackson, *Classical Electrodynamics.* Wiley, 1999.

[36] http://photon-science.desy.de/research/students___teaching/primers/synchrotron_radiation/index_eng.html.

[37] G. V. Marr, *Handbook on Synchrotron Radiation: Vacuum Ultraviolet and Soft X-ray Processes.* Elsevier, 2013, vol. 2.

[38] P. Schmüser *et al.*, *Ultraviolet and soft X-ray free-electron lasers: introduction to physical principles, experimental results, technological challenges.* Springer Science & Business Media, 2008, vol. 229.

[39] S. Corde *et al.*, "Femtosecond x rays from laser-plasma accelerators," *Reviews of Modern Physics*, vol. 85, no. 1, p. 1, 2013.

[40] V. Ginsburg *et al.*, "Radiation of a uniformly moving electron due to its transition from one medium into another," *Zhurnal eksperimentalnoi i teoreticheskoi fiziki*, vol. 16, no. 1, pp. 15–28, 1946.

[41] M. L. Ter-Mikaelian, *High energy electromagnetic processes in condensed media.* Wiley, 1972.

[42] L. Wartski, "Etude du rayonnement de transition optique produit par des électrons d'énergie 30 à 70 mev. application aux diagnostics de faisceaux de particules chargées," Ph.D. dissertation, 1976.

[43] P. Rullhusen *et al.*, *Novel radiation sources using relativistic electrons: from infrared to x-rays.* World Scientific, 1998, vol. 4.

[44] J. Ashley, "Transition radiation from thin foils due to non-normally incident electrons," *Physical Review*, vol. 155, no. 2, p. 208, 1967.

[45] K. Mc Donald, "Transition radiation as a beam diagnostic," Joseph Henry Laboratories, Princeton University, Princeton, NJ 08544, Tech. Rep., 1989.

[46] B. Yang, "A Design Report for the Optical Transition Radiation Imager for the LCLS Undulator," SLAC, Tech. Rep., 2005.

[47] G. Garibian, "Contribution to the theory of transition radiation," *Sov. Phys. JETP*, vol. 6, no. 6, p. 1079, 1958.

[48] V. Pafomov, "Radiation of a charged particle in the presence of a separating boundary," in *Nuclear Physics and Interaction of Particles with Matter.* Springer, 1971, pp. 25–157.

[49] L. D. Landau *et al.*, "The classical theory of fields," 1971.

[50] L. Wartski *et al.*, "Thin films on linac beams as non-destructive devices for particle beam intenstty, profile, centertng and energy monitors," *IEEE Transactions on Nuclear Science*, vol. 22, no. 3, pp. 1552–1557, 1975.

[51] G. Kube, "Imaging with optical transition radiation, transverse beam diagnostics for the xfel," *TESLA-FEL Report*, vol. 1, p. 2008, 2008.

[52] S. Casalbuoni *et al.*, "Far-infrared transition and diffraction radiation," *Tesla Report*, vol. 15, no. 2005, p. 2012, 2005.

[53] E. Chiadroni *et al.*, "Effects of transverse electron beam size on transition radiation angular distribution," *Nuclear Instruments and Methods in Physics Research Section A: Accelerators, Spectrometers, Detectors and Associated Equipment*, vol. 673, pp. 56–63, 2012.

[54] V. Verzilov, Private Communication.

[55] A. Cianchi *et al.*, "Transverse emittance diagnostics for high brightness electron beams," *Nuclear Instruments and Methods in Physics Research Section A*, 2016.

[56] H. Loosy *et al.*, "Observation of coherent optical transition radiation in the lcls linac," in *Presented at*, no. SLAC-PUB-13395, 2008.

[57] S. Wesch *et al.*, "Observation of coherent optical transition radiation and evidence for microbunching in magnetic chicanes," in *Proc. 31st Int. Free-Electron Laser Conf., Liverpool, UK*, 2009, pp. 619–622.

[58] L. G. Sukhikh *et al.*, "Backward transition radiation in the extreme ultraviolet region as a tool for the transverse beam profile diagnostic," *Physical Review Special Topics-Accelerators and Beams*, vol. 17, no. 11, p. 112805, 2014.

[59] B. Schmidt *et al.*, "Longitudinal bunch diagnostics using coherent transition radiation spectroscopy," *arXiv preprint arXiv:1803.00608*, 2018.

[60] F. Giorgianni *et al.*, "Tailoring of highly intense thz radiation through high brightness electron beams longitudinal manipulation," *Applied Sciences*, vol. 6, no. 2, p. 56, 2016.

[61] M. Marongiu *et al.*, "Design issues for the optical transition radiation screens for theeli-np compton gamma source," in *7th International Particle Accelerator Conference (IPAC'16), Busan, Korea, May 8-13*, 2016, pp. 118–121.

[62] E. Bravin, "Thermal Analysis of OTR Screens for CTF3," CERN, Geneva, Switzerland, Tech. Rep. CTF3-Note-019, March 2001.

[63] V. Balandin *et al.*, "Survival and thermal heating of materials for the OTR screens at the TTF2," 2001, unpublished.

[64] M. Ross *et al.*, "A Very High Resolution Optical Transition Radiation Beam Profile Monitor," in *BIW2002*, 2002.

[65] P. Piot *et al.*, "High-current CW beam profile monitors using transition radiation at CEBAF," in *AIP Conference Proceedings*, vol. 390, no. 1. AIP, 1997, pp. 298–305.

[66] J. Frisch *et al.*, "Electron beam diagnostics and feedback for the LCLS-II," in *Proceedings of FEL2014, Basel, Switzerland*, 2014, pp. 666–671.

[67] F. Cioeta *et al.*, "Thermal simulations for optical transition radiation screen for eli-np compton gamma source," in *5th Int. Beam Instrumentation Conf.(IBIC'16), Barcelona, Spain, Sept. 13-18*, 2016, pp. 537–540.

[68] F. Cioeta *et al.*, "Spot size measurements in the eli-np compton gamma source," in *5th Int. Beam Instrumentation Conf.(IBIC'16), Barcelona, Spain, Sept. 13-18*, 2016, pp. 533–536.

[69] M. Marongiu *et al.*, "Beam energy measurements with a optical transition radiation for the eli-np compton gamma source," in *6th Int. Beam Instrumentation Conf.(IBIC'17), Grand Rapids, MI, USA, August 20-24*, 2017.

[70] "Material parameters taken by Matweb," http://www.matweb.com/.

[71] A. Variola, "Utilisation du rayonnement optique pour l'etude des caracteristiques spatiotemporelles d'un faisceau d'electrons. Application a TTF," Ph.D. dissertation, Universite de Paris-Sud, France, 1998.

[72] E. Bravin *et al.*, "OTR Studies for the High Charge CTF3 Beam," in *Particle Accelerator Conference, PAC 2003. Proceedings of*, vol. 4. IEEE, 2003, pp. 2464–2466.

[73] J. E. Shigley, *Shigley's mechanical engineering design*. Tata McGraw-Hill Education, 2011.

[74] G. Yahr, "Fatigue design curves for 6061-t6 aluminum," vol. 45221, pp. 1–15, 1993.

[75] M. J. Kirkham, "Advances in ultra-high cycle fatigue," 2002.

[76] "Zemax Optic Studios," https://www.zemax.com/products/opticstudio.

[77] A. Giribono *et al.*, "6d phase space electron beam analysis and machine sensitivity studies for eli-np gbs," *Nuclear Instruments and Methods in Physics Research Section A*, vol. 829, pp. 274–277, 2016.

[78] "Thorlabs app note: "resolution test targets"," https://www.thorlabs.com/newgrouppage9.cfm?objectgroup_id=4338.

[79] B. Yang, "A design report for the optical transition radiation imager for the lcls undulator," SLAC National Accelerator Laboratory (SLAC), Tech. Rep., 2010.

[80] X. Z. Qiu *et al.*, "Proposal for using optical transition radiation for electron beam alignment and emittance measurement for the free emittance measurement for the free electron laser experiments at atf," Brookhaven National Lab., Tech. Rep., 1994.

[81] C. Wiebers *et al.*, "Scintillating screen monitors for transverse electron beam profile diagnostics at the european xfel," *proceedings of IBIC*, 2013.

[82] S. T. Boogert *et al.*, "Micron-scale laser-wire scanner for the kek accelerator test facility extraction line," *Physical Review Special Topics-Accelerators and Beams*, vol. 13, no. 12, p. 122801, 2010.

[83] W. Graves *et al.*, "A high resolution electron beam profile monitor and its applications," in *AIP Conference Proceedings*, vol. 451, no. 1.   AIP, 1998, pp. 206–213.

[84] K. Nakamura *et al.*, "Broadband single-shot electron spectrometer for gev-class laser-plasma-based accelerators," *Review of Scientific Instruments*, vol. 79, no. 5, p. 053301, 2008.

[85] Y. Glinec *et al.*, "Absolute calibration for a broad range single shot electron spectrometer," *Review of scientific instruments*, vol. 77, no. 10, p. 103301, 2006.

[86] D. Filippetto *et al.*, "Phase space analysis of velocity bunched beams," *Physical Review Special Topics-Accelerators and Beams*, vol. 14, no. 9, p. 092804, 2011.

[87] A. Mostacci *et al.*, "Chromatic effects in quadrupole scan emittance measurements," *Physical Review Special Topics-Accelerators and Beams*, vol. 15, no. 8, p. 082802, 2012.

[88] A. Cianchi *et al.*, "Six-dimensional measurements of trains of high brightness electron bunches," *Physical Review Special Topics-Accelerators and Beams*, vol. 18, no. 8, p. 082804, 2015.

[89] P. Antici *et al.*, "Laser-driven electron beamlines generated by coupling laser-plasma sources with conventional transport systems," *Journal of Applied Physics*, vol. 112, no. 4, p. 044902, 2012.

[90] A. R. Rossi *et al.*, "The external-injection experiment at the sparc_lab facility," *Nuclear Instruments and Methods in Physics Research Section A*, vol. 740, pp. 60–66, 2014.

[91] M. Castellano, "A new non-intercepting beam size diagnostics using diffraction radiation from a slit," *Nuclear Instruments and Methods in Physics Research Section A: Accelerators, Spectrometers, Detectors and Associated Equipment*, vol. 394, no. 3, pp. 275–280, 1997.

[92] P. Catravas *et al.*, "Beam profile measurement at 30 gev using optical transition radiation," 1999.

[93] C. Thomas *et al.*, "Single shot emittance measurement from beam size measurement in a drift section," in *Proceedings of the 1st International Particle Accelerator Conference*, 2010, p. 1167.

[94] U. Iriso *et al.*, "Experience with yag and otr screens at alba," *SAT*, vol. 5, no. 2008.10, p. 15, 2009.

[95] "Yag screen," http://www.crytur.cz/materials/yagce/.

[96] A. Lumpkin, "Time-resolved imaging for the aps linac beams." Argonne National Lab., IL (US), Tech. Rep., 1998.

[97] G. Kube *et al.*, "Inorganic scintillators for particle beam profile diagnostics of highly brilliant and highly energetic electron beams," *Proceedings of IPAC2012, New Orleans, Lousiana, USA*, vol. 28, 2012.

[98] G. Kube *et al.*, "Transverse beam profile imaging of few-micrometer beam sizes based on a scintillator screen," 2016.

[99] M. Castellano *et al.*, "Spatial resolution in optical transition radiation beam diagnostics," *Physical Rewiew Special Topics - Accelerators and Beams*, vol. 1, 1998.

[100] A. Potylitsyn, "Image of optical diffraction radiation (odr) source and spatial resolution of odr beam profile monitor," in *Advanced Radiation Sources and Applications.* Springer, 2006, pp. 149–163.

[101] D. Xiang *et al.*, "Theoretical considerations on imaging of micron size electron beam with optical transition radiation," *Nuclear Instruments and Methods in Physics Research Section A: Accelerators, Spectrometers, Detectors and Associated Equipment*, vol. 570, no. 3, pp. 357–364, 2007.

[102] A. Aryshev *et al.*, "Sub-micrometer resolution transverse electron beam size measurement system based on optical transition radiation," in *IPAC 2011-2nd International Particle Accelerator Conference*, 2011, pp. 1964–1966.

[103] K. Kruchinin *et al.*, "Extremely low emittance beam size diagnostics with sub-micrometer resolution using optical transition radiation," 2013.

[104] G. Kube *et al.*, "Transverse beam profile diagnostics using point spread function dominated imaging with dedicated de-focusing," 2013.

[105] I. A. Artyukov, "Schwarzschild objective and similar two-mirror systems," in *Short-Wavelength Imaging and Spectroscopy Sources*, vol. 8678. International Society for Optics and Photonics, 2012, p. 86780A.

[106] G. Kube *et al.*, "Micron-scale vertical beam size measurements based on transition radiation imaging with a schwarzschild objective," 2016.

[107] M. Marongiu *et al.*, "Design of the diagnostic stations for the eli-np compton gamma source," in *9th Int. Particle Accelerator Conf.(IPAC'18), Vancouver, BC, Canada, April 29-May 4, 2018*, 2018, pp. 2173–2176.

[108] B. Bolzon *et al.*, "Very high resolution optical transition radiation imaging system: Comparison between simulation and experiment," *Physical Review Special Topics - Accelerators and Beams*, vol. 18, no. 8, pp. 1–8, 2015.

[109] J. Wolfenden *et al.*, "COMPARISON OF OPTICAL TRANSITION RADIATION SIMULATIONS AND THEORY," in *9th Int. Particle Accelerator Conf.(IPAC'18), Vancouver, BC, Canada, April 29-May 4, 2018*, pp. 455–457.

[110] F. G. Bisesto *et al.*, "Zemax simulations describing collective effects in transition and diffraction radiation," *Optics Express*, vol. 26, no. 4, p. 5075, 2018.

[111] M. Marongiu *et al.*, "Energy measurements by means of transition radiation in novel linacs," *Nuclear Instruments and Methods in Physics Research Section A: Accelerators, Spectrometers, Detectors and Associated Equipment*, 2018.

[112] M. Ferrario *et al.*, "Sparc_lab present and future," *Nuclear Instruments and Methods in Physics Research Section B*, vol. 309, pp. 183–188, 2013.

[113] "General particle tracer code," http://www.pulsar.nl/gpt/.

[114] "Elegant code," https://www.aps.anl.gov/Accelerator-Operations-Physics/Software#elegant.

[115] D. Alesini *et al.*, "Design of high gradient, high repetition rate damped c-band rf structures," *Physical Review Accelerators and Beams*, vol. 20, no. 3, p. 032004, 2017.

[116] A. Mosnier, "Instabilities in linacs," CERN, Tech. Rep., 1993.

[117] X. Artru *et al.*, "Experimental investigations on geometrical resolution of optical transition radiation (OTR)," *Nuclear Instruments and Methods in Physics Research Section A*, vol. 410, no. 2, pp. 148–158, 1998.

[118] G. Vignola, "Dafne: the first f-factory," in *Proceedings of the fifth European Particle Accelerator Conference (EPAC'96), Sitges (Barcelona), Institute of Physics Publishing, Bristol, Philadelphia*, 1996, p. 22.

[119] A. Ghigo *et al.*, "Daϕne beam instrumentation," in *AIP Conference Proceedings*, vol. 451, no. 1. AIP, 1998, pp. 183–190.

[120] A. Stella, Private Communication.

List of Figures

List of Tables